Pergamon

Int. J. Solids Structures Vol. 35, No. 22, pp. 2975–3001, 1998

0020–7683/98 $19.00 + .00

PII: S0020–7683(97)60353–3

A NUMERICAL INVESTIGATION OF PENETRATION IN MULTILAYERED MATERIAL/STRUCTURE SYSTEMS

H. D. ESPINOSA,* S. DWIVEDI, P. D. ZAVATTIERI and G. YUAN
School of Aeronautics and Astronautics, Purdue University, West Lafayette, IN 47907-1282, U.S.A.

(*Received* 6 *August* 1997; *in revised form* 12 *November* 1997)

Abstract—The response of multilayered ceramic/steel targets to high velocity impact and penetration has been investigated through finite element simulations. A multiple-plane microcracking model has been used to describe the inelastic constitutive behavior of ceramics in the presence of damage. The model has been integrated into the finite element code EPIC95, which possesses contact and erosion capabilities particularly suitable for ballistic simulations. The integrated code has been used to analyze the depth of penetration (DOP) and interface defeat (ID) ceramic target configurations. Parametric analyses have been carried out to establish the effect of ceramic materials, target configuration design for ceramic confinement, diameter/length (d/L) ratio of the penetrator, material erosion threshold levels and the use of a shock attenuator on the response of multilayered targets subjected to high velocity impact. The response characteristics are established in terms of the parameters which can be measured experimentally. The analyses show that the integrated code is able to predict the response of ceramic targets in confirmation with experimental findings reported in the literature. The penetration process is found to be less dependent on the ceramic materials as usually assumed by most investigators. By contrast, the penetration process is highly dependent on the multilayered configuration and the target structural design (geometry, and boundary conditions). From a simulation standpoint, it has been found that the erosion parameter plays an important role in predicting the deformation history and interaction of the penetrator with the target. These findings show that meaningful lightweight armor design can only be accomplished through a combined experimental/numerical study in which relevant ballistic materials and structures are *simultaneously* investigated.

1. INTRODUCTION

The response of armor structures to high velocity impact and penetration depends on projectile geometry, geometry and arrangement of target plates, physical and mechanical properties of projectile and target materials, impact velocity and angle of impact. It is crucial for structures used in defense applications, e.g., armor plates, to defeat projectile adhering to specified design criteria. The design criteria may be a maximum depth of penetration, tolerable or no damage to the rear of the structure, etc. Multilayered material arrangement for target structures has proved efficient for the purpose. Apart from these basic mechanics requisites, advanced applications need minimum weight design of structures. Lately, ceramics have gained popularity in this context due to their low density and high compressive strength. But limitations arise due to their low tensile strength and brittle behavior. Tensile rarefaction waves, generated on the surface and at material interfaces, cause abrupt failure and fracture of the material. Hence, subsequent resistance to penetration, in the fragmented stage, is a strong function of confining pressure.

There have been several efforts to experimentally design suitable multi-layered structures with ceramic plates. The focus of these experiments has been to minimize ceramic damage and flow to maximize penetration resistance. Shockey *et al.* (1990) studied failure of confined ceramic targets penetrated by long tungsten rods. Their target configuration was essentially the so-called depth of penetration (DOP) configuration with the addition of a thin steel cover plate. This confinement produces a comminuted zone, at the penetrator

* Author to whom correspondence should be addressed. Fax: 001 765 494 0307.

nose, consisting of finely fragmented ceramic. It was rightly envisaged by Shockey and co-workers that unless the fractured material moves out of penetrator path, penetration cannot occur. Penetration can progress only if the comminuted material flows laterally under high pressure. They recovered the samples and analyzed the different kinds of cracks generated at various stages, concluding that friction, wear, and flow govern the resistance offered by confined ceramics to penetration. These observations gave rise to the belief that ceramic internal friction is one of the most important ballistic material properties. This belief motivated pressure–shear studies on ceramics and ceramic powders, Klopp and Shockey (1991), Espinosa and Clifton (1991), Sairam and Clifton (1994).

Another detailed experimental study for designing suitable multi-layered ceramic targets was carried out by Hauver and co-workers (1993, 1994), Rapacki *et al.* (1996). They found that the performance of ceramic targets during penetration depends on the nature of ceramic confinement. They proposed a new structure known as interface defeat (ID) ceramic target configuration. In this configuration, a thick and stiff cover plate is utilized as a shield to the ceramic. A thin plate of light weight material, e.g., graphite, is placed between the ceramic and the cover plate to allow the lateral flow of the penetrator. The penetrator nose is deformed and spread laterally at the interface resulting in the geometric transformation of penetrator from rod to disk. The transformation preserves and expands the loading area on the ceramic target resulting in improved ceramic confinement with minimum motion of the fragmented material in the so-called Mescall zone. If the stiffness of the steel cover plate is adequate, the penetrator lateral flow, at the ceramic/graphite interface, prevents the motion of ceramic fragments and therefore defeats the tungsten projectile.

Recently, Orphal *et al.* (1996, 1997a, b) studied the response of confined AlN, SiC and B_4C ceramics during long rod penetration at velocities ranging from 1.5 to 5 km/s. They measured substantial data with the help of flash X-rays, e.g., penetration depth, rate of rod consumption, mass efficiency of the ceramic target, etc.

Although numerical analyses of high velocity impact and penetration have been carried out for quite some time, their application in analyzing the response of ceramic targets is scarce. The key issue is the appropriate modeling of the complex constitutive behavior of ceramics in the presence of cracks. Attempts have been made to model the inelastic constitutive behavior of ceramics in the presence of cracks, and to validate the models through simulation of plate and rod impact experiments. Addessio and Johnson (1989) presented a microphysical model to describe the confined behavior of ceramics. The inelastic strains in their model are assumed to be caused by microcracking. Cracks are allowed to slide under compression and open under tension. Damage is determined in terms of a crack density parameter whose evolution is described through a failure surface based on energy balance. Following these ideas, few other phenomenological models have been developed to describe the inelastic constitutive behavior of ceramics (Johnson and Cook, 1985; Steinberg, 1992).

Rajendran and Grove (1992) proposed a model considering microcrack nucleation and growth, and pore collapse. Damage is defined in terms of an average crack density which is treated as an internal state variable. The reduction in stiffness due to microcracking is modeled using damage moduli whose evolution under compressive, as well as tensile loading, is formulated based on the generalized Griffith criterion. Pore collapse is modeled using viscoplastic equations derived from Gurson's pressure dependent yield function (Gurson, 1977). The model was implemented in the commercial finite element code EPIC-2 (Johnson and Stryk, 1986) and simulations of a steel rod penetrating a ceramic plate were performed. Despite the fact that this model of damage is isotropic, the stress profile obtained in the simulations compared reasonably well with the experimental results.

Curran *et al.* (1990) proposed a computational model to describe penetration of ceramic targets through a multiple-plane phenomenological model. In their model, the deviatoric stress in the comminuted material is used to describe inelasticity and flow. Pressure is calculated with the help of the standard Mie–Gruneisen equation of state for the solid intact material. A continuum porous compaction model accounting for the applied shear strain is used for its calculation in the comminuted zone. Their yield function accounts for damage as well as Coulomb's friction. A tensile fracture model is used to allow the

separation of fragmented pieces. Curran and co-workers identified their model parameters from pressure–shear impact experiments and performed simulations of the confined ceramic targets tested by Shockey *et al.* (1990). Based on the simulations, they concluded that confining pressure and intergranular friction in the comminuted material are the key factors governing the penetration resistance of the confined ceramics. One of the major disadvantages in the use of their model is that the phenomenological parameters introduced to describe the various inelastic processes are difficult to identify experimentally. Moreover, the material response is obtained by adding the effect of various inelastic mechanisms independently. This approach requires the definition of a transition from intact to comminuted material based on a somewhat arbitrary criterion.

To overcome the limitations of the phenomenological models previously mentioned, and in particular, damage isotropy and difficulties in determining model parameters, Espinosa (1995), derived a multiple-plane microcracking model (MPM) based on the theory of micromechanics of solids. In the MPM model, the constitutive response of the material is obtained from fundamental quantities that can be determined experimentally such as grain size, and fracture toughness. In addition, since the dynamic growth of microcracks is described independently on each orientation, damage induced anisotropy and rate effects are naturally incorporated in the model. More details on the MPM model are given in the next section.

Apart from the development of models describing the constitutive behavior of brittle materials, and the numerical simulation of plate and rod impact experiments, not many studies have been carried out to establish the structural performance of multi-layered ceramic targets. It is known that differences in ceramic response to multi-axial loading are a function of processing route and resulting material microstructure. However, it is unclear to what extent. It has been argued that studies on the shear resistance of comminuted ceramics are fundamental to the prediction of target penetration. By contrast, Hauver's findings revealed that the key is to design armor structures that avoid large amounts of ceramic flow. Therefore, it is clear that a combined experimental/computational approach is crucial to understand optimum design of light weight armor with ceramic materials. Such studies can provide insight into the relevance of measurable quantities such as velocities, strains and stresses in material/structure performance, and can also lead to the answer of fundamental questions such as the role of the ceramic microstructure in armor performance. However, due to the complexity of the problem, the kind of sensors to be used and their locations remain illusive. In previous work, measurement type and location were decided based on intuition and experience derived from past experiments. Any lack of information was manifested in terms of repeating the experiments, which are very expensive and time consuming. There is also the possibility of arriving at inappropriate conclusions if the selected variables are not measured with proper accuracy.

We believe that the numerical simulations of ballistic events, with powerful algorithms and models, can overcome the difficulties mentioned in the above paragraph. The temporal and spatial variation of all field variables during the penetration process can be obtained. However, an accurate model to describe the inelastic constitutive behavior of ceramics needs to be included together with an accurate description of target geometry and boundary conditions. After model validation, with experimental data obtained independently, the simulations can be used effectively to determine the crucial parameters to be measured, their peak magnitude and location. By virtue of this, the kind of sensors to be employed and their location in the target can be predetermined with confidence. This translates directly into the optimization of ceramic target design.

As a first step in the design of ballistic experiments, the authors have implemented the multiple-plane microcracking model developed by Espinosa (1995), into the finite element software EPIC95 to describe the inelastic behavior of ceramics. A detailed parametric study is carried out for the penetration of the two configurations, namely, DOP and ID, of multi-layered confined ceramic target plates impacted by long rod tungsten penetrators. In these simulations, particular emphasis is placed on understanding the history of measurable quantities as a function of target configuration, ceramic type, use of shock attenuators, and ceramic confinement.

2. NUMERICAL SIMULATION MODEL

Large scale simulations of ballistic penetration are very difficult because they require the formulation of material models capable of representing material behavior at high rate of deformations under multiaxial dynamic loading. Inelasticity and fracture, as well as interface behavior between structural components, need to be modeled. To avoid circularity, deformation and fracture properties, at high pressures and strain rates, need to be determined independently through model parameter identification on selected plate and rod impact tests. It is the objective of the analyst to formulate models that can describe the physics present in penetration events with the simplest possible models, but at the same time, formulate models that can predict shear or damage localization, failure model transition from ductile to brittle or vice versa, and at the same time be robust from a computational standpoint.

In this section, we briefly describe the multiple-plane microcracking model developed by Espinosa (1995) to simulate damage and fragmentation of brittle materials. Salient features of the finite element code EPIC95, and the integration of the model in the code are also discussed.

2.1. *Multiple-plane microcracking model*

The multiple-plane microcracking model developed by Espinosa (1995), is based on the nucleation and dynamic growth of penny-shaped defects. See also Espinosa (1992), Espinosa *et al.* (1992). The basic assumption in the model is that microcracking and/or slip can occur on a discrete number of orientations as shown in Fig. 1.

Slip plane properties, viz., friction, initial defect size and density, and their evolution are independently computed on each plane. The macroscopic response of the material is computed by additive decomposition of the strain tensor into elastic and inelastic parts. The inelastic strains are assumed to be caused solely by the presence of microcracks in the solid.

For a representative volume B of an elastic solid containing penny-shaped microcracks, the average inelastic strains are given by

$$\varepsilon_{ij}^{c} = \sum_{k=1}^{9} N^{(k)} S^{(k)} \frac{1}{2} (\bar{\mathbf{b}}_i^{(k)} \mathbf{n}_j^{(k)} + \mathbf{n}_i^{(k)} \bar{\mathbf{b}}_j^{(k)}) \tag{1}$$

where N and S are the density and surface area, of the microcrack, respectively, $\mathbf{n}$ is the unit normal vector on the surface of the crack and $\bar{\mathbf{b}}$ is the average displacement jump vector across S, while the superindex k is used to label their values for each orientation.

If the resolved normal traction acting on the microcrack on orientation k is tensile, the average displacement jump vector resulting from the applied stress field σ_{ij} is given by

$$\bar{\mathbf{b}}_i^{(k)} = \frac{1}{S^{(k)}} \int_{S^{(k)}} \bar{\mathbf{b}}_i^{(k)} \, \mathrm{d}S = \frac{16(1-\nu^2)}{3E(2-\nu)} a^{(k)} (2\sigma_{ij} \mathbf{n}_j^{(k)} - \nu \sigma_{jl} \mathbf{n}_j^{(k)} \mathbf{n}_l^{(k)} \mathbf{n}_i^{(k)}), \tag{2}$$

in which E and ν are the Young's modulus and Poisson's ratio of the uncracked solid and a is the radius of the penny-shaped microcrack. By contrast, the microcracks close if the resolved normal stress is compressive. The average displacement jump in this case is given by

$$\bar{\mathbf{b}}_i^{(k)} = \frac{32(1-\nu^2)}{3\pi E(2-\nu)} a^{(k)} \mathbf{f}_i^{(k)}. \tag{3}$$

Here, $\mathbf{f}$ is the effective shear traction vector whose value for orientation k is given by

$$\mathbf{f}_i^{(k)} = (\tau^{(k)} + \mu\sigma_n^{(k)})\mathbf{n}_{\tau i}^{(k)}, \tag{4}$$

where, μ is the internal friction coefficient of the microcrack faces, τ and σ_n are the resolved shear and normal stresses, respectively, and $\mathbf{n}_\tau$ is the unit vector in the direction of the resolved shear traction. Embodied in the above equation is the notion that $\mathbf{f}$ provides the effective driving force for the sliding of the microcracks. If $\tau^{(k)} \leqslant \mu\sigma_n^{(k)}$ a sticking condition occurs. Hence, irreversible displacement jumps develop making the deformation process strongly nonlinear and history dependent.

In order to compute the inelastic strain tensor at all times, it becomes necessary to follow the evolution of the microcrack radius a in the selected orientations. Following Freund (1990), an equation of evolution for a, in the case of mixed mode loading can be derived as,

$$\dot{a}^{(k)} = m^{\pm} c_R [1 - (K_{IC}/\mathbf{K}_{eff}^{(k)})^{n\pm}] \geqslant 0, \tag{5}$$

in which $n^{\pm}$ and $m^{\pm}$ are phenomenological material constants which may have different values in tension and compression, c_R is the Rayleigh wave speed, K_{IC} is the material toughness and $\mathbf{K}_{eff}$ is the effective stress intensity factor. For mixed mode conditions, $\mathbf{K}_{eff}$ for the particular orientation k is derived by considering the average energy release rate $\mathcal{G}$ associated with the increase in radius of the microcracks, a, and is given by,

$$\mathcal{G}^{(k)} = \frac{1}{2\pi}\int_0^{2\pi} \frac{1-\nu^2}{E}[K_I^2 + K_{II}^2 + K_{III}^2/(1-\nu)]\,d\theta \tag{6}$$

from which the following expression for $\mathbf{K}_{eff}$ is obtained,

$$\mathbf{K}_{eff}^{(k)} = \sqrt{\frac{\mathcal{G}^{(k)}E}{1-\nu^2}}. \tag{7}$$

The general structure of these constitutive equations corresponds to that of a solid with damage-induced anisotropic stress–strain relations allowing for elastic degradation. If the material is subjected to a predominantly tensile stress state, microcracks along the orientation perpendicular to the direction of the maximum tensile stress will grow as per eqn (5). Significant dilation is expected in this case due to mode I crack opening. If a predominantly compressive state of stress with shear is imposed, then crack opening is inhibited, but inelasticity is manifested by the growth of the penny-shaped cracks in modes II and III.

Hence, in contrast to the scalar representations of damage, e.g., Rajendran (1992) and Rajendran and Grove (1992), the present model is broad enough to allow the examination of damage induced anisotropy, pressure dependence, and damage localization in the interpretation of impact and ballistic penetration experiments. In particular, the effective behavior of the solid is predicted to be rate dependent due to crack kinetics effects. From a computational standpoint, this ensures numerical reliability and mesh-size independence (Needleman, 1988; Espinosa, 1989). This is in contrast to quasi-static formulations of damage for which the governing equations become ill-posed in the softening regime, e.g., Sandler and Wright (1984). Furthermore, the model is based on the mechanics of solids with cracks and consequently, model parameters can be identified from knowledge of material microstructure and crack densities obtained in plate and/or rod impact recovery experiments.

2.2. *Computational Code, EPIC95*

EPIC95 is a special purpose Lagrangian finite element code particularly suitable for two and three dimensional simulations of high velocity impact phenomena, Johnson (1976), and Johnson *et al.* (1986, 1987, 1994). The code discretizes the impactor and target structure

spatially into constant strain triangles or tetrahedrons. The equations of motion are integrated explicitly using a variable time stepping algorithm. The deviatoric strains and stresses are found in the updated coordinates after making corrections for rigid body rotations. The shock pressure is calculated using the Mie–Gruneisen equation of state and shock Hugoniot parameters of the materials. Both linear, as well as quadratic artificial viscosity, are added to smear the shock front and improve the stability of the explicit integration. The contact between impactor and target is analyzed with the help of an explicit contact algorithm. The code allows for penetration and perforation by eroding elements from the impactor surface as well as the target structure, Johnson and Stryk (1987). The erosion is modeled based on the criterion that elements do not contribute to the dynamic equilibrium if their effective plastic or cracking strain reaches a critical value. If an element shares nodes at the surface and satisfies the criterion, then the stresses in it are brought to zero and the element is allowed to disappear. But, its mass can still be preserved at the nodes.

The code has been successful in simulating high velocity impact of many impactor–target configurations at normal as well as oblique incidences. Elements composed of four cross triangles are used in two dimensional calculations. These elements offer infinite resistance as their volume tends to zero and have been successfully employed in numerical simulations of ballistic penetration. As a result, it does not lead to negative Jacobian due to high element distortion. This eliminates the need of remeshing, which is necessary when higher order elements are used in ballistic penetration problems. However, the code has the capability of analyzing only metal to metal impact and limited capability of analyzing metal to concrete impact.

The above features of the code make it highly suitable for simulating the response of ceramic targets wherein the penetration and perforation are imminent. The microcracking model described in Section 2.1 has been integrated into the code for the purpose. The integrated code has been used successfully to carry out series of parametric analyses as described in the following section. Thus, the integration imparts further capability to the EPIC code for simulating the penetration of the ceramic targets.

3. ANALYSES AND RESULTS

3.1. *Geometry and materials definition*

The integrated code has been used to carry out axisymmetric two dimensional analyses of high velocity impact and penetration of multilayered ceramic target plates. The DOP and ID configurations are shown in Figs 2 and 3, respectively, with the notation for dimensions. The penetrator in all the cases is a cylindrical long rod with flat ends made of Tungsten heavy alloy (WHA).

Two types of ceramics, alumina (Al_2O_3) and silicon carbide (SiC), have been considered for each type of target plate. The steel casing for both targets, cover plate and sleeve for ID targets is RHA steel. The ID target has also been analyzed with a shock attenuator made of alternate layers of aluminum and PMMA materials. Analyses are carried out for three ratios of the penetrator diameter to length (d/L), namely, 0.025, 0.05 and 0.1. The normal impact velocity in all the cases is 1500 m/s.

Table 1 summarizes the dimensions of the impactor and target structures for various analyses, while the material properties are given in Table 2 and Table 3. The values of effective plastic strain used as erosion parameter are given in Table 4. It needs to be pointed out that it is difficult to fix the dimensional criterion for comparing the response of the DOP vis-á-vis ID targets due to the presence of the cover plate and interface layer. In the present analyses, the two targets are compared for the same initial surface area, i.e. the outside diameter D_p is kept the same for the two target structures. Also, due to the unavailability of data, the inelastic model parameters for both ceramics, Al_2O_3 and SiC, have been kept the same as obtained by modeling of rod on rod impact experiments, see Espinosa *et al.* (1995, 1997a).

3.2. *Results and discussion*

The results obtained from the analyses are given below in terms of the effect of various factors on the response of multilayered confined ceramic target plates to impact and

Table 1. Dimensions of impactor and target plate used in analyses

Run No.	Dimensions (mm)										
	d	L	D_p	T_{hp}	D_c	T_c	T_{cp}	D_i	T_i	T_s	d/L
dop1	7.874	78.74	203.2	127.0	76.2	50.8	—	—	—	—	0.1
dop2	7.874	78.74	203.2	127.0	76.2	50.8	—	—	—	—	0.1
dop3	3.937	78.74	215.9	127.0	76.2	50.8	—	—	—	—	0.05
id1	5.0	100.0	215.9	50.8	72.0	25.4	17.05	82.0	2.0	5.0	0.05
id2	5.0	100.0	215.9	50.8	72.0	25.4	17.05	82.0	2.0	5.0	0.05
id3	5.0	100.0	215.9	50.8	72.0	25.4	17.05	82.0	2.0	5.0	0.05
id4	5.0	100.0	215.9	50.8	72.0	25.4	17.05	82.0	2.0	5.0	0.05
id5	5.0	100.0	215.9	50.8	72.0	25.4	17.05	82.0	2.0	5.0	0.05
id6	5.0	100.0	215.9	50.8	72.0	25.4	17.05	82.0	2.0	5.0	0.05
id7	2.5	100.0	215.9	50.8	72.0	25.4	17.05	82.0	2.0	5.0	0.025
id8	10.0	100.0	215.9	50.8	72.0	25.4	17.05	82.0	2.0	5.0	0.1

Table 2. Material properties of Al_2O_3 and SiC used in analyses with microcracking multiple-plane model

Material properties	Symbol	Units	Al_2O_3	SiC
Young's modulus	E	GPa	374.0	429.7
Poisson's ratio	ν	—	0.22	0.15
Density	ρ_0	Kg/m^3	3890.0	3177.0
Internal friction coefficient	μ	—	0.1	0.1
Wave speed	c_R	m/s	5000.0	5000.0
Critical stress intensity factor	k_{IC}	MPa$\sqrt{m}$	4.0	4.0
Initial crack radius	a_0	μm	1.0	1.0
Crack density in different orientations	$N^{(1)}$	/m^3	1.0E+12	1.0E+12
	$N^{(2)}$	/m^3	0.0	0.0
	$N^{(3)}$	/m^3	1.0E+12	1.0E+12
	$N^{(4)}$	/m^3	0.0	0.0
	$N^{(5)}$	/m^3	0.0	0.0
	$N^{(6)}$	/m^3	0.0	0.0
	$N^{(7)}$	/m^3	5.0E+10	5.0E+10
	$N^{(8)}$	/m^3	0.0	0.0
	$N^{(9)}$	/m^3	0.0	0.0
Mie–Gruneisen equation of state (Johnson, 1994) $P = (K_1\mu_s + K_2\mu_s^2 + K_3\mu_s^3)(1-\Gamma\mu_s/2) + \Gamma E_s(1+\mu_s)$ $\mu_s = \rho/\rho_0 - 1$; $\Gamma = K_1\alpha/\rho C$				
Equation of state parameters	K_1	GPa	204.0	204.0
	K_2	GPa	0.0	0.0
	K_3	GPa	0.0	0.0
Gruneisen coefficient	Γ	—	0.0	0.0
Coefficient of thermal expansion	α	—	0.0	0.0
Specific heat	C	—	920.0	920.0
Cut-off tension limit	P_{min}	GPa	68.95	68.95
Linear artificial viscosity	C_L	—	0.0	0.0
Quadratic artificial viscosity	C_Q	—	0.0	0.0

penetration. The effects are discussed in terms of parameters amenable to measurement with the help of interferometers and in-material gauges.

3.2.1. *Effect of ceramic material.* The DOP target plate has been analyzed with both Al_2O_3 and SiC ceramics for a penetrator with $d/L = 0.05$. The erosion parameter has been chosen as 1.5 and analyses are carried out till the elapsed time of 150 μs. The penetration of the two confined ceramics at three time cycles together with a plot of effective plastic/cracking strain are shown in Fig. 4.

Table 3. Properties of other materials used in analyses with EPIC model

Material properties	Symbol	Units	WHA	RHA Steel	Graphite	Aluminum	PMMA
Shear modulus	G	Gpa	124.1	77.5	36.0	27.58	2.25
Density	ρ_0	Kg/m^3	16,980.0	7823.0	1800.0	2704.0	1185.0
Modified Johnson–Cook Model (Johnson, 1995) $\sigma = [C_1 + C_2\varepsilon^N][1 + C_3 \ln \dot{\varepsilon}^*][1 - T^{*M}] + C_4 P$ $\dot{\varepsilon}^* = \dot{\varepsilon}/\dot{\varepsilon}_0$; $\dot{\varepsilon}_0 = 1.0$/s							
Model constants	C_1	GPa	1.506	1.4	0.579	0.324	0.19
	C_2	GPa	0.177	1.8	0.0	0.114	0.0
	N	—	0.12	0.768	1.0	0.42	1.0
	C_3	GPa	0.016	0.005	0.0	0.002	0.0
	M	—	1.0	1.17	0.0	1.34	0.0
	C_4	—	0.0	0.0	1.0	0.0	0.0
	σ_{max}	GPa	0.0	0.0	2.0	0.0	0.0
EOS parameters	K_1	GPa	302.1	163.9	72.0	76.74	6.2
	K_2	GPa	469.8	294.4	0.0	128.3	29.5
	K_3	GPa	334.9	500.0	0.0	125.1	13.4
Gruneisen coefficient	Γ	—	1.43	1.16	0.24	2.0	0.0
Coefficient of thermal expansion	α	—	0.0	0.0	2.016E−4	0.0	2.016E−4
Specific heat	C	—	134.5	477.8	1340.0	896.2	1340.0
Cut-off tension limit	P_{min}	GPa	68.95	68.95	68.95	68.95	68.95
Linear artificial viscosity	C_L	—	0.2	0.2	0.2	0.0	0.2
Quadratic artificial viscosity	C_Q	—	4.0	4.0	4.0	0.0	4.0

Table 4. Erosion parameter used for different target configurations

Run No.	Ceramic	Interface type	Value of effective plastic strain used as erosion parameter: Cover plate	Ceramic	Block plate	Graphite
dop1	SiC	−2	—	1.5	1.5	—
dop2	Al_2O_3	−2	—	3.0	1.5	—
dop3	Al_2O_3	−2	—	1.5	1.5	—
id1	Al_2O_3	−2	1.5	3.0	1.5	1.5
id2	SiC	−2	1.5	1.5	1.5	1.5
id3	Al_2O_3	−2	3.0	3.0	3.0	3.0
id4	Al_2O_3	−2	1.5	1.5	1.5	1.5
id5	Al_2O_3	−2	3.0	3.0	3.0	3.0
id6	Al_2O_3	−2	9.0	9.0	9.0	9.0
id7	Al_2O_3	−2	1.5	1.5	1.5	1.5
id8	Al_2O_3	−2	1.5	1.5	1.5	1.5

It is seen that the response of both ceramics to penetration is similar without much appreciable difference. At the early stages of penetration, at about 10 μs, severe shock wave damage is observed in front of the penetrator nose. The penetrator and crater in the two cases appear similar in size and shape. The nose reaches the bottom ceramic–steel interface at about 45 μs in both cases. This indicates that the rate of penetration for Al_2O_3 and SiC ceramics is approximately the same. The deformed shape of the penetrator and crater shape continue to be similar for both types of ceramics. In the final stages of penetration (t = 150 μs), the residual length of the penetrator is similar for the two cases. However, the crater shape in the case of SiC target is larger than that in Al_2O_3, specially at the ceramic–steel interface. This may be due to the higher wave speed in SiC which results in more time for wave interactions at the interface.

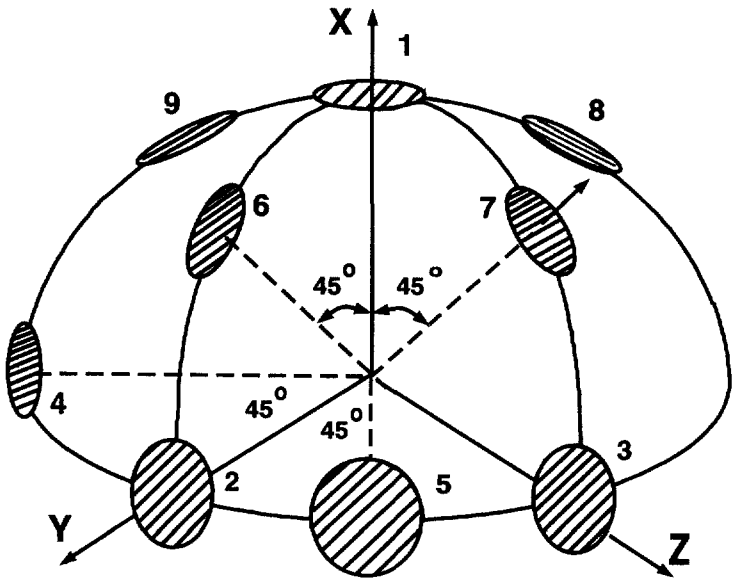

Fig. 1. Schematic of microcracking multiple-plane model.

The temporal history of field variables, such as stress and velocity, has been stored at discrete time intervals. They are compared in terms of the model parameters at locations in which experimental measurements can be obtained. Particle velocities can be measured with interferometric techniques and stresses can be measured with in-material manganin/constantan gages, see Brar *et al.* (1997). Figure 5 shows the penetrator tail velocity for both cases, which can also be experimentally monitored (Espinosa *et al.* 1996a, 1997a). It is found that apart from a small difference at the late stages (t = 130–150 μs), the tail velocity is almost identical for both ceramics. The velocity decreases slowly initially, followed by a sharp decrease between 100 and 130 μs. This phenomena is related to the penetrator loss of mass and kinetic energy. Moreover, a well defined velocity structure is observed with a duration corresponding to wave propagation between penetrator nose and tail. This feature has been measured experimentally by Espinosa *et al.* (1997a).

Figure 6 shows a comparison of stress histories at the centroid of an element located at the ceramic–steel interface (henceforth referred as interface stress). Once again, this stress can be measured in experiments. It is seen that the shock stress in both Al_2O_3 and SiC is very low initially, about 2 GPa, and becomes close to zero after approximately 5 μs. At about 18 μs, the axial stress becomes compressive again, with a value of about 2 GPa, and close to zero once more until approximately 30 μs. This phenomenon can be explained by the increase in crater dimension, ahead of the penetrator, due to inertia effects. In fact, after the accumulation of wave damage, upon impact, erosion removes elements that have achieved the erosion criterion resulting in the loss of contact between penetrator and ceramic target. Once erosion of damaged material stops, the impactor once again makes contact with the ceramic target and sends a second stress wave. Pressure and shear waves initiate damage once more. As can be observed in Fig. 6, this even occurs three times in the present simulation. In the last of such events, the penetrator is close to the ceramic–steel back plate interface and therefore, the axial stress increases to 9 and 6 GPa in SiC and Al_2O_3, respectively, at about 35 μs. Since the thickness of ceramic material, responsible for shock attenuation, is now reduced, higher peak stresses are recorded. Subsequent erosion and contact give still higher stresses with a peak magnitude of 24 GPa immediately before the penetrator nose reaches the interface. The element is eroded immediately after that, and the interface is exposed with the axial stress dropping to zero, as seen in Fig. 6.

The higher stress value in the SiC ceramic may be due to its higher strength and Hugoniot elastic limit (HEL). Despite some noticeable differences in stress history, the

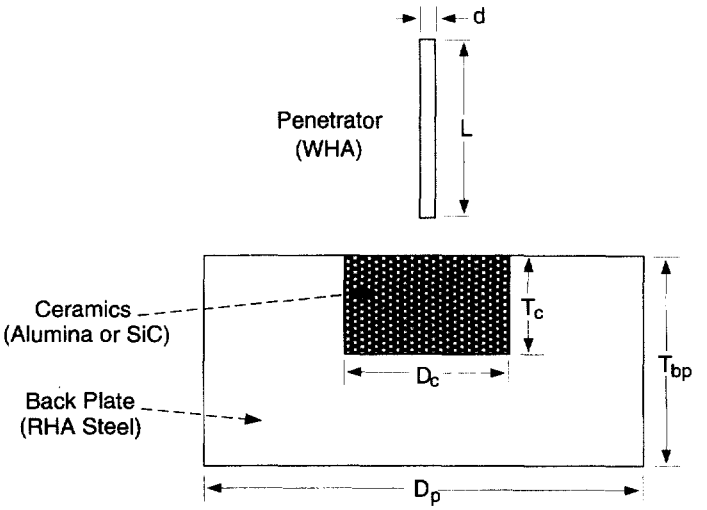

Fig. 2. Depth of penetration configuration.

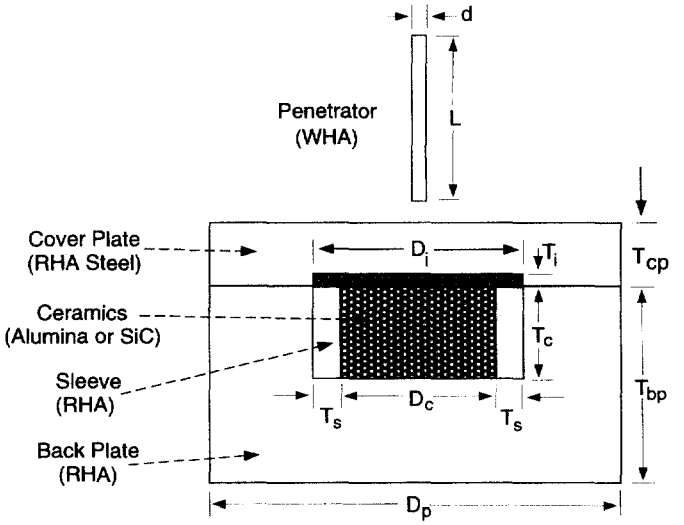

Fig. 3. Interface-defeat configuration.

overall penetration history displays little dependence on the ceramic elastic properties. A similar result is obtained for the ID configuration.

3.2.2. *DOP vs ID configurations.* In order to compare the response of the DOP and ID configurations, analyses have been carried out with a penetrator having a d/L of 0.05. Al_2O_3 is used in both configurations with the erosion parameter set as 1.5. Figure 7 shows the penetration event together with the plot of effective plastic/cracking strain at three different time cycles. The variation in penetrator tail velocity, for the two configurations, is shown in Fig. 8.

It is seen that the penetrator reaches the ceramic–steel interface, after defeating the ceramic plate, at 55 μs in the case of DOP. In the ID configuration, the nose of the penetrator reaches the surface of the ceramic at 27 μs after defeating the cover plate. At this time, the penetrator tail velocity is identical for both types of structures. Subsequently, it reduces significantly more in the case of ID than in the case of DOP. The wave damage in the ceramic for the ID configuration is less than it is for the DOP configuration as expected due to the variation in ceramic confinement. This is confirmed by the smaller

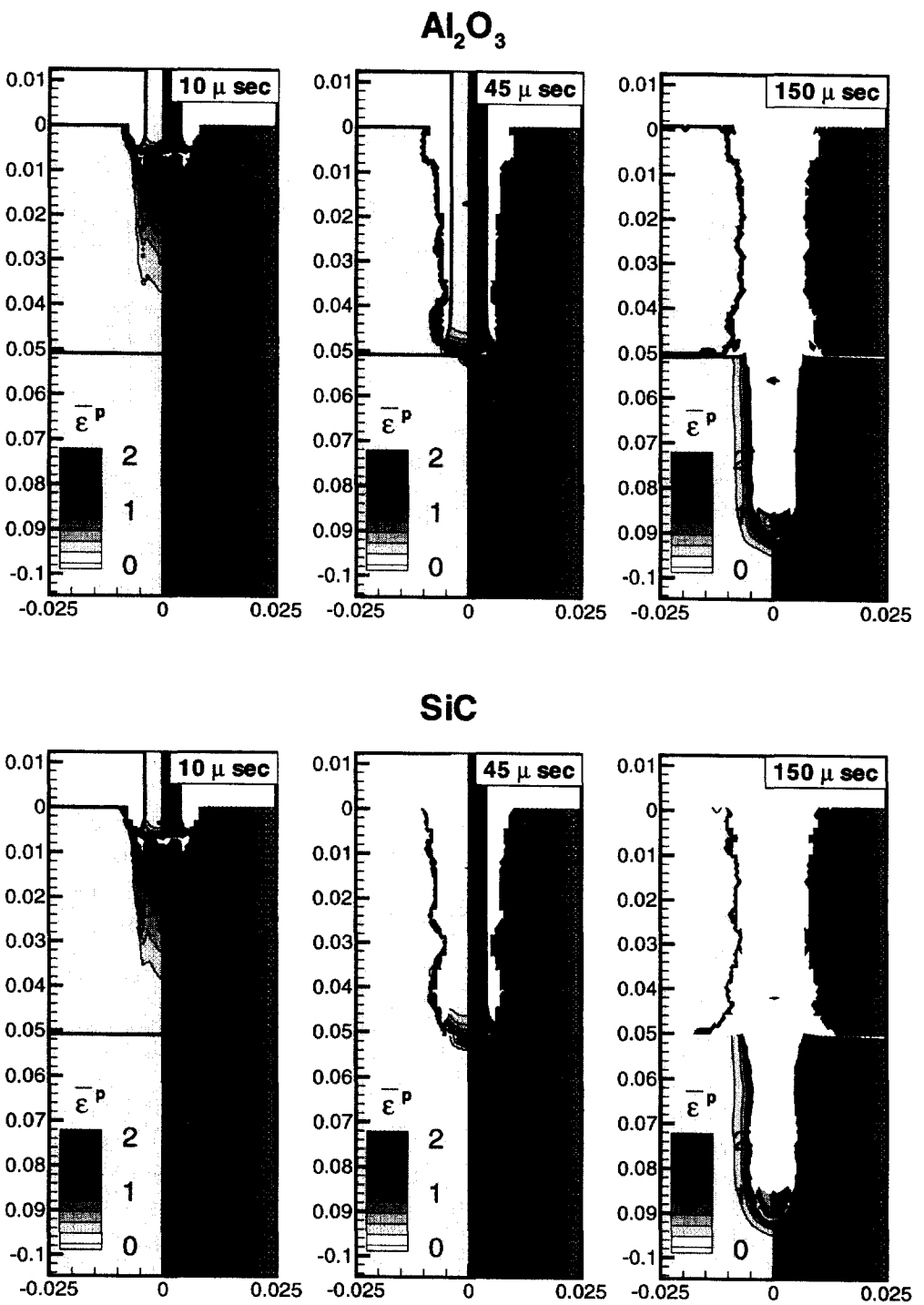

Fig. 4. Penetration and effective plastic/cracking strain for DOP configuration with confined alumina and silicon carbide ceramics ($d/L = 0.05$, erosion = 1.5).

crater dimension for ID vis-á-vis DOP. Hence, the model predicts a superior behavior of the multi-layered ceramic target structures in confirmation with the experimental evidence. However, Hauver's experimental observation that the penetrator nose is deformed and spread laterally during interface defeat is not obtained in the present simulation. The reason is that EPIC95 cannot preserve elements with large accumulated plastic/cracking

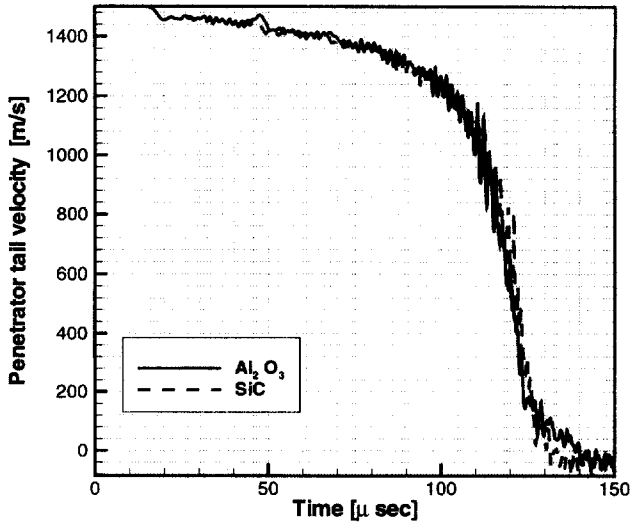

Fig. 5. Penetrator tail velocity for DOP configuration with confined Al_2O_3 and SiC ceramics ($d/L = 0.05$, erosion = 1.5).

deformations. Hence, the spread zone cannot fully develop due to penetrator and target erosion. However, flattening of the penetrator nose and delay penetration into the ceramic plate are observed in the numerical results.

3.2.3. *Effect of penetrator* d/L *ratio.* In practice, the scalability of experimental results to field application is very crucial. One is always interested, during development stages, to derive useful information for field design from laboratory results. It is well established that penetrability increases with the reduction in penetrator d/L ratio for the same kinetic energy. In this study, analyses have been carried out for the ID configuration at three d/L values of 0.025, 0.05 and 0.1. As mentioned earlier the erosion parameter is kept constant as 1.5. The impact velocity in all cases is 1500 μs so that the kinetic energy of the penetrator is not preserved.

Figures 9–11 show penetration at different cycles together with the plot of plastic strain rate obtained from analyses for the three d/L ratios. At the early stages of penetration, about 10 m/s in Fig. 9, the location of maximum plastic strain rate is dependent on the diameter of the impactor. It is highly localized in the case of the smallest d/L ratio. As the ratio increases, the plastic strain rate contours are observed to become more planar. Due to a higher shock wave amplitude, in the case of d/L of 0.1, a significant accumulation of plastic strain rate in the graphite layer is observed. When the penetrator nose reaches the graphite–ceramic interface, as shown in Fig. 10, the strain rate in the ceramic is very similar for all three ratios, even though the penetrator with higher d/L carries more kinetic energy. At the late stages of penetration, shown in Fig. 11, the penetrator nose displays slightly different shapes for the different d/L ratios. The penetrator with larger d/L develops a more triangular shape and lower strain rates within its body.

In order to study damage in the ceramic target, maximum normal and shear stress contours have been plotted in Figs 12–14 for the three ratios of d/L at the instant when the nose of the impactor reaches the graphite–ceramic interface. This stage of penetration is chosen for comparison because it corresponds to the critical time at which ceramic damage and confinement govern the resistance to further penetration. It is seen that the maximum normal stress increases with the d/L ratio. However, the shear stress, which governs ceramic damage, is distributed differently in the three cases indicating significant differences in the damage zone. If a critical shear stress of 1 GPa is assumed to dictate damage onset in the ceramic, it can be seen that the extent of ceramic damage is less for the ratio of 0.1 as compared to the other two smaller d/L ratios. The bulb shape of the damage at d/L ratio of 0.025 matches with that reported by Hauver for the same ratio. As the ratio increases,

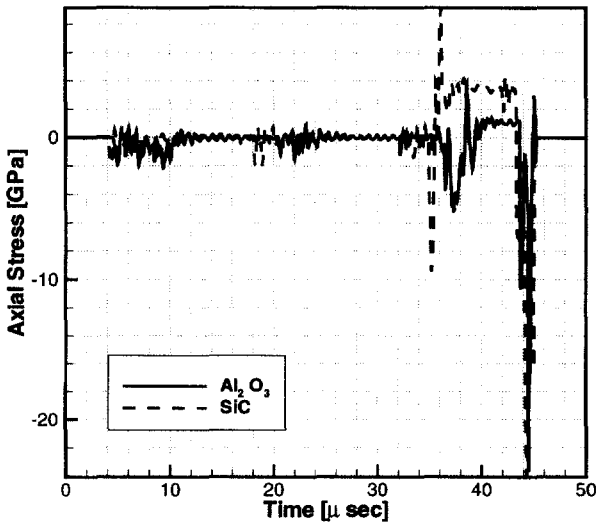

Fig. 6. Axial stress at the ceramic–steel interface for DOP configuration with confined alumina and silicon carbide ceramics (d/L = 0.05, erosion = 1.5).

the damage zone becomes more planar and shifts downward from the surface of the ceramic. One may infer from these results that the damage zone is initiated at the graphite–ceramic interface and propagates downwards leaving behind the comminuted zone.

In order to study the overall penetration characteristics, the normal stress at the interface between ceramic and RHA steel is plotted in Fig. 15. It is seen that the timing for the stress to achieve its maximum value at this location varies with d/L ratio. This indicates variation in the penetration speed as noted earlier. The time for achieving a peak stress is found to be 80, 57 and 50 μs for the ratios 0.025 to 0.05 and 0.1, respectively. The corresponding penetration speed can be calculated to be 0.56, 0.78 and 0.89 Km/s, respectively. Obviously, the penetrator has a larger kinetic energy for higher values of d/L and so the penetration speed is also higher. The maximum compressive stress for the d/L ratios of 0.025 and 0.05 is almost identical to 26 GPa while it is 20 GPa for the d/L of 0.1. Due to a stronger shock wave amplitude for the highest d/L ratio, the damage zone reaches the interface earlier than in the other cases, and therefore it limits the maximum stresses that can be achieved in the ceramic.

Figure 16 shows the variation of the penetrator tail velocity for the three d/L ratios. The penetrator tail velocity for d/L = 0.025 reduces slowly till 100 μs followed by a sharp reduction to zero due to the complete defeat of the penetrator. The penetrator tail velocity for the other two ratios is almost indistinguishable, see Fig. 16. The penetrator perforates the target plate with a residual penetrator tail velocity of 1200 m/s for both d/L ratios.

Figure 17 shows the velocity history at the back surface of the target plate. As seen, the back of the target surface has a small oscillating value of 40 m/s for the d/L ratio of 0.025 as the penetrator is finally stopped. For the other two ratios, 0.05 and 0.1, the velocity of the rear surface increases as the penetrator reaches the target back surface. Finally, the surface is perforated at which instant, the velocity suddenly drops to zero. Maximum velocities of 880 and 840 are obtained for d/L ratios of 0.05 and 0.1, respectively. Due to differences in penetration speed, the rising part of the axial velocity starts at about 50 and 75 μs for d/L of 0.1 and 0.05, respectively. It should be noted that such velocity histories can be obtained interferometrically as explained in Espinosa *et al.* (1997a).

In spite of the fact that the kinetic energy of the penetrator has not been preserved in the analyses, the above results indicate that the penetrators with smaller d/L ratio have better penetration characteristics. This result is in agreement with scaling predictions of the eroding rod model or Tate's model. According to this model, penetration is proportional to penetrator length if all other properties are held constant. Moreover, the calculations show there is no defeat of the penetrator with the largest d/L ratio, due to its higher kinetic

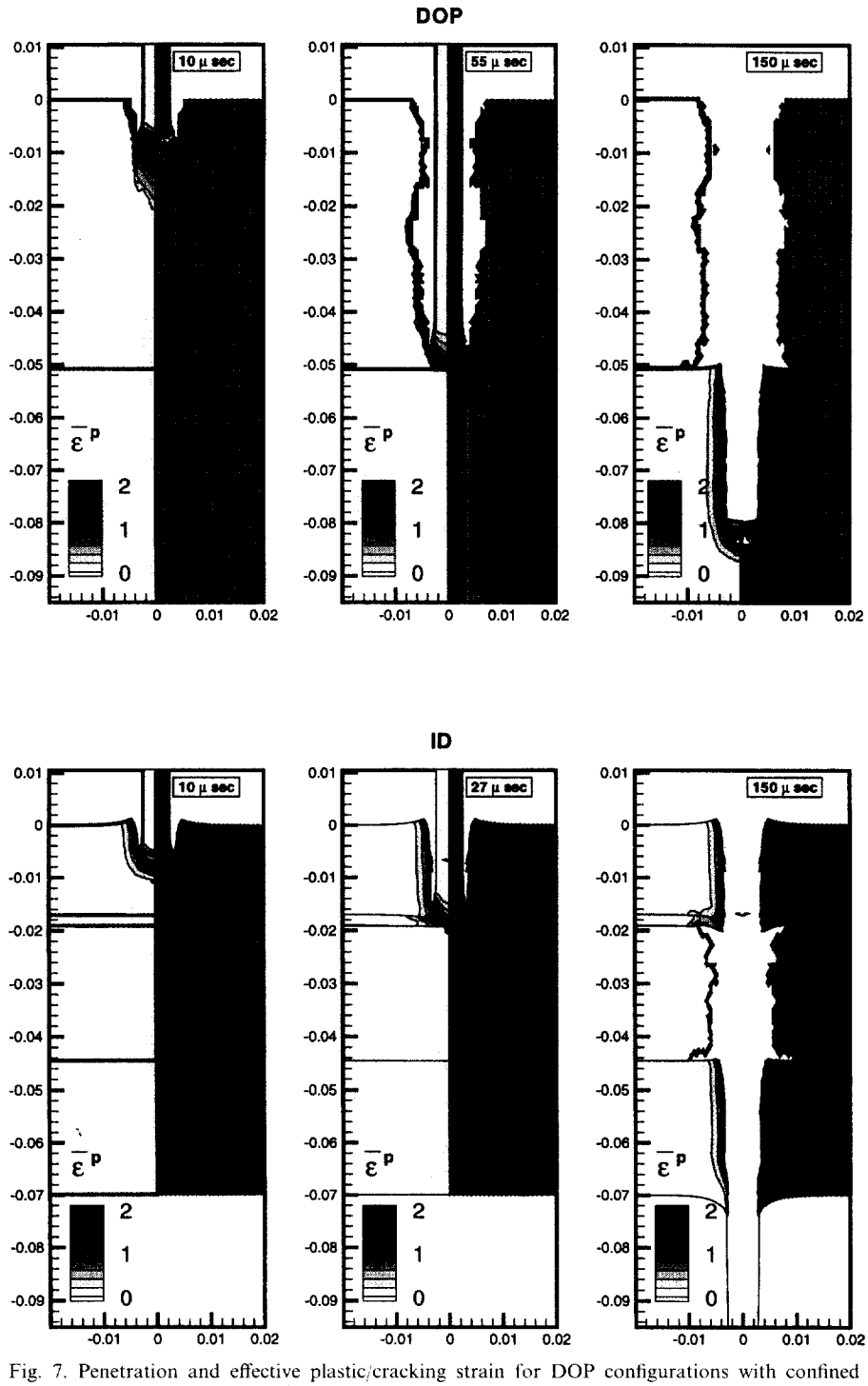

Fig. 7. Penetration and effective plastic/cracking strain for DOP configurations with confined alumina ($d/L = 0.05$, erosion = 1.5).

energy, which confirms the importance of yet another scaling parameter, i.e., the ceramic plate thickness.

3.2.4. *Effect of erosion parameter.* As mentioned earlier, EPIC95 employs a critical effective plastic/cracking strain as erosion parameter for eroding elements from the impactor as well as target structure. A higher value of the erosion parameter means that it is more difficult to erode material but at the same time results in higher mesh distortion and smaller

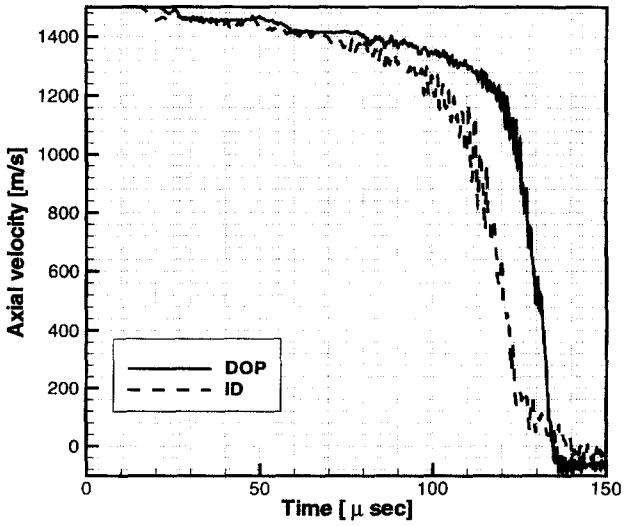

Fig. 8. Penetrator tail velocity for DOP and ID configurations with confined alumina (d/L = 0.05, erosion = 1.5).

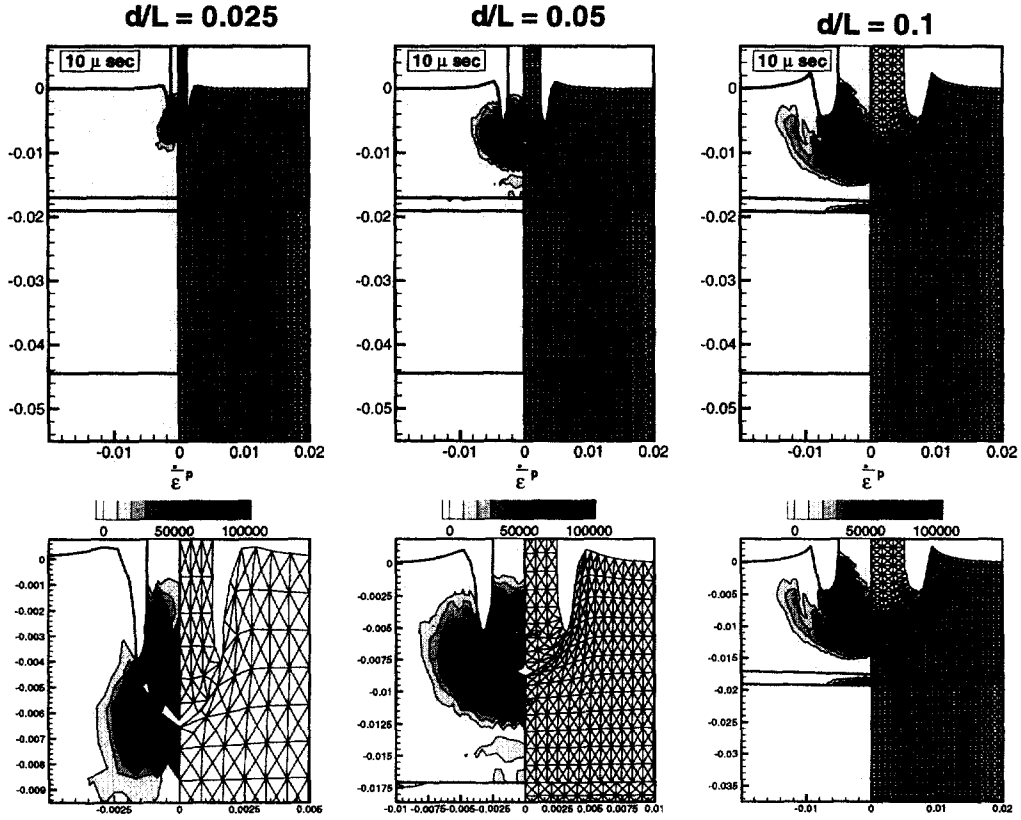

Fig. 9. Penetration and plastic strain rate for ID configuration with confined alumina and different d/L ratios (erosion = 1.5, the lower plots are the enlarged view of the deformed zone).

time steps. In all the above analyses, its value has been kept constant as 1.5. In order to study its effect on penetration, the ID target plate with Al_2O_3 ceramic has been analyzed for two additional values of the erosion parameter, namely 3.0 and 9.0, with the d/L ratio set in all cases to 0.05.

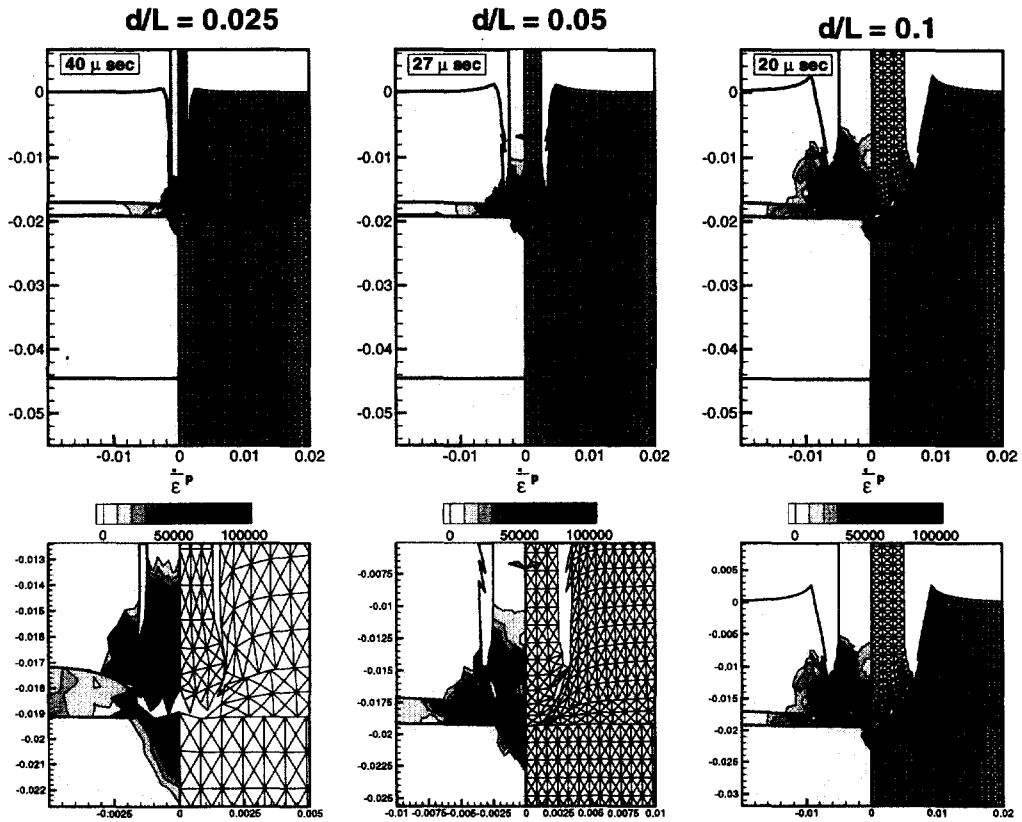

Fig. 10. Penetration and plastic strain rate for ID configuration with confined alumina and different d/L ratios (erosion = 1.5).

Figure 18 shows the penetration at different cycles for the three erosion values. At 10 μs, it is observed that as the material becomes more difficult to be removed with increasing values of the erosion parameter, the penetrator material flows upwards and develops a triangular nose. The sharpness of the nose increases as the penetration continues, facilitating further penetration by focusing the inelastic deformation right ahead of the penetrator. As a result, the penetrator reaches the graphite–ceramic interface at 27, 24 and 16 m/s for erosion values of 1.5, 3.0 and 9.0, respectively. The difference in the nose shape provides different initial conditions when the penetrator hits the ceramic–graphite interface. Despite the faster rate of penetration, with increasing erosion value, overall penetration of the target plate is not achieved when the erosion value is set to 9.

The erosion parameter affects not only the deformed shape of the penetrator but also the whole history of stresses and particle velocities. Figure 19 shows the axial stress history at the ceramic–steel interface for the three values of erosion. At an erosion value of 1.5, the compressive stress increases to a value of 6 GPa before the penetrator reaches the interface. When the tip of the penetrator hits the interface at 57 μs, the stress increases to 27 GPa. As the erosion value increases to 3, the timing of the penetrator reaching the interface remains more or less the same, i.e., 57 μs. However, the peak stress is only about 16 GPa. When the erosion value is increased to 9, the stress at the interface becomes compressive much earlier than in the other cases and reverses from compressive 10 GPa to tensile 9 GPa at about 40 μs. This feature of stress reversal is not observed for the smaller two values of the parameter. When the tip of the penetrator reaches the interface, the stress reverses back to a compressive stress of about 13 GPa which is smaller than the stress in the cases of erosion values of 1.5 and 3.

The peculiar penetration response is further shown in the plot of the penetrator tail velocity shown in Fig. 20. The tail velocity reduces gradually in the beginning with a well

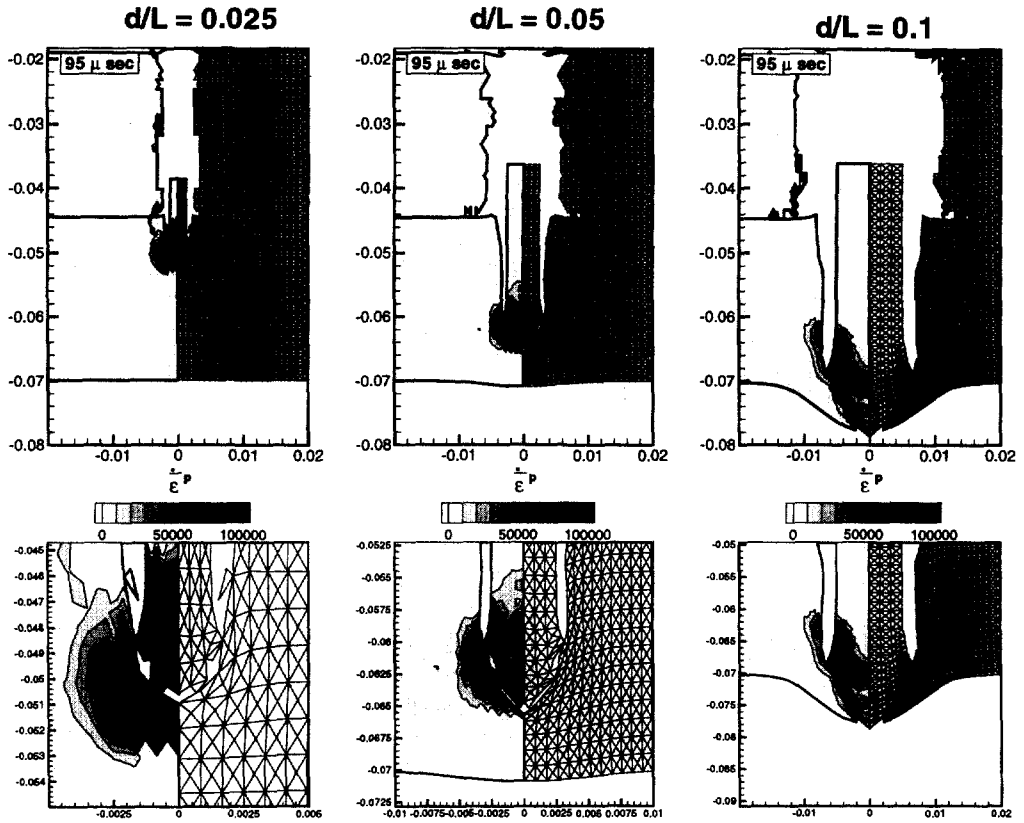

Fig. 11. Penetration and plastic strain rate for ID configuration with confined alumina and different d/L ratios (erosion = 1.5).

defined structure corresponding to the transient time for waves to travel from the penetrator nose to its tail. When the erosion parameter is set to 1.5, a residual velocity of 1140 m/s is predicted. For higher erosion values, the tail velocity drops suddenly after 100 and 80 μs for 3.0 and 9.0, respectively. Residual tail velocities of about 1140, 340 and 170 m/s are numerically predicted for erosion values of 1.5, 3.0 and 9.0, respectively. This indicates that even though higher rates of penetration are predicted with increasing values of the erosion parameter, the overall resistance to penetration increases significantly.

3.2.5. *Effect of shock attenuator.* The above results show that the shape of the penetrator nose plays an important role in the penetration process and also governs the peak stress in the various layers. Based on these ideas, Hauver proposed to use a multi-layered shock attenuator to flatten the penetrator nose and reduce the peak stress in the ceramic. Moreover, when the penetrator reaches the graphite layer, a rounded shape is desired to facilitate lateral flow, when the penetrator reaches the graphite–ceramic interface. In order to study shock attenuation effects, an analysis has been carried out for the ID configuration of the ceramic target with shock attenuator. The d/L ratio of the penetrator has been chosen as 0.05 and the erosion value as 1.5. The shock attenuator is made of 20 layers of luminum and PMMA, arranged alternately, with each layer having a thickness of 1 mm.

Figure 21 shows the penetration of the multilayered target with and without attenuator at the early and late stages. In the early stages, at 10 μs, it is seen that the nose is indeed rounded during the penetration time through the attenuator. This potentially results in a better resistance to penetration. As shown in the later stages, the ceramic cavity appears smaller when the attenuator is used. In Fig. 22, a peak compressive stress of 22 GPa is obtained at the graphite–ceramic interface when the attenuator is used, while a value of 27 GPa is obtained in the absence of shock attenuator. Also, a delay in 17 μs is observed in

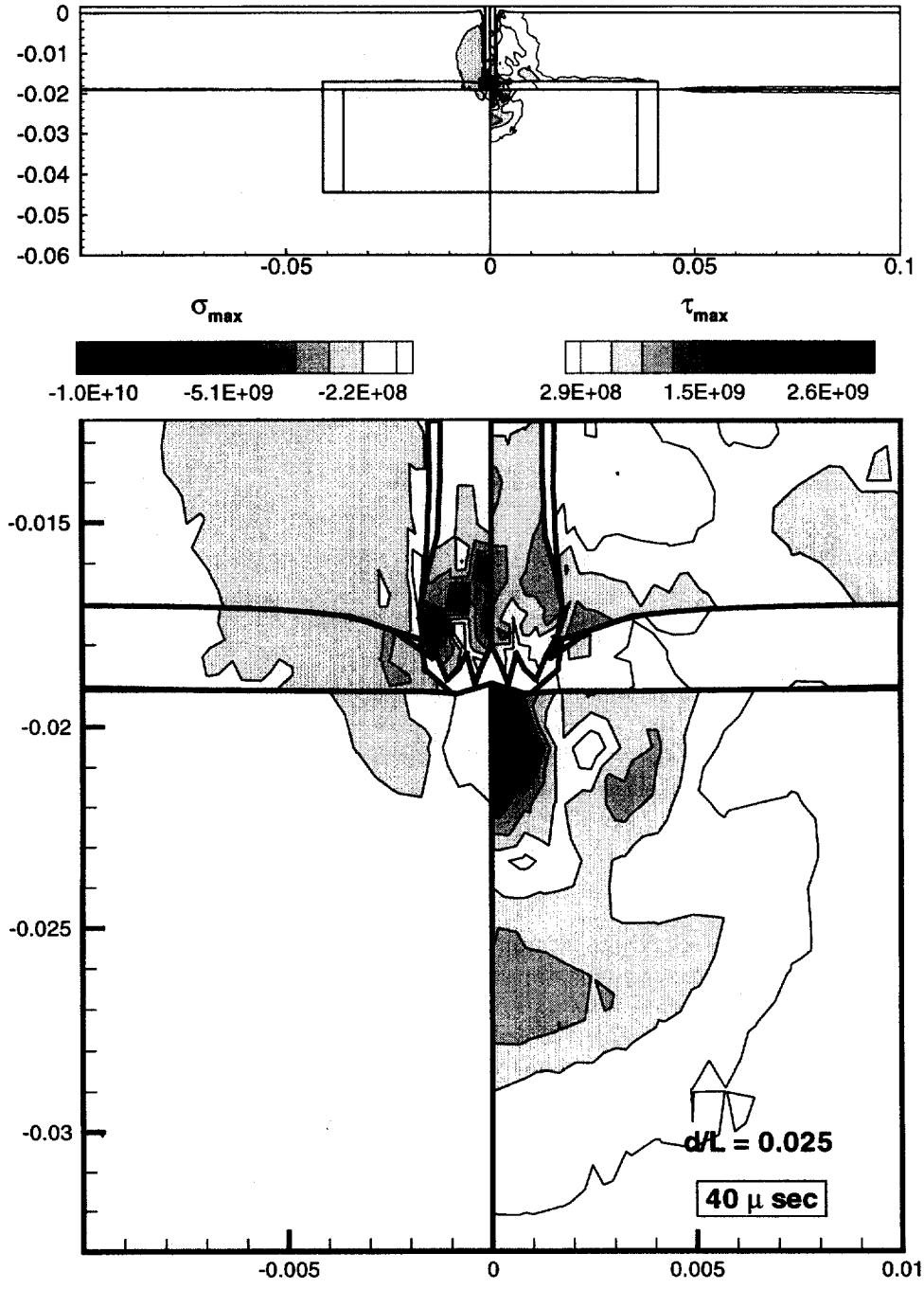

Fig. 12. Contours of maximum principal stress and maximum shear stress for the ID configuration with $d/L = 0.025$ and erosion = 1.5.

the peak stress due to the penetration through the attenuator. The improved resistance of the target with the shock attenuator is also observed from the variation of the penetrator tail velocity shown in Fig. 23. The use of the shock attenuator reduces the penetrator tail velocity, although this is expected by the addition of the shock attenuator plate. Probably, the most important observation is that shock stress and penetrator nose can be modified by tailoring the cover plates laid on top of the ceramic plate.

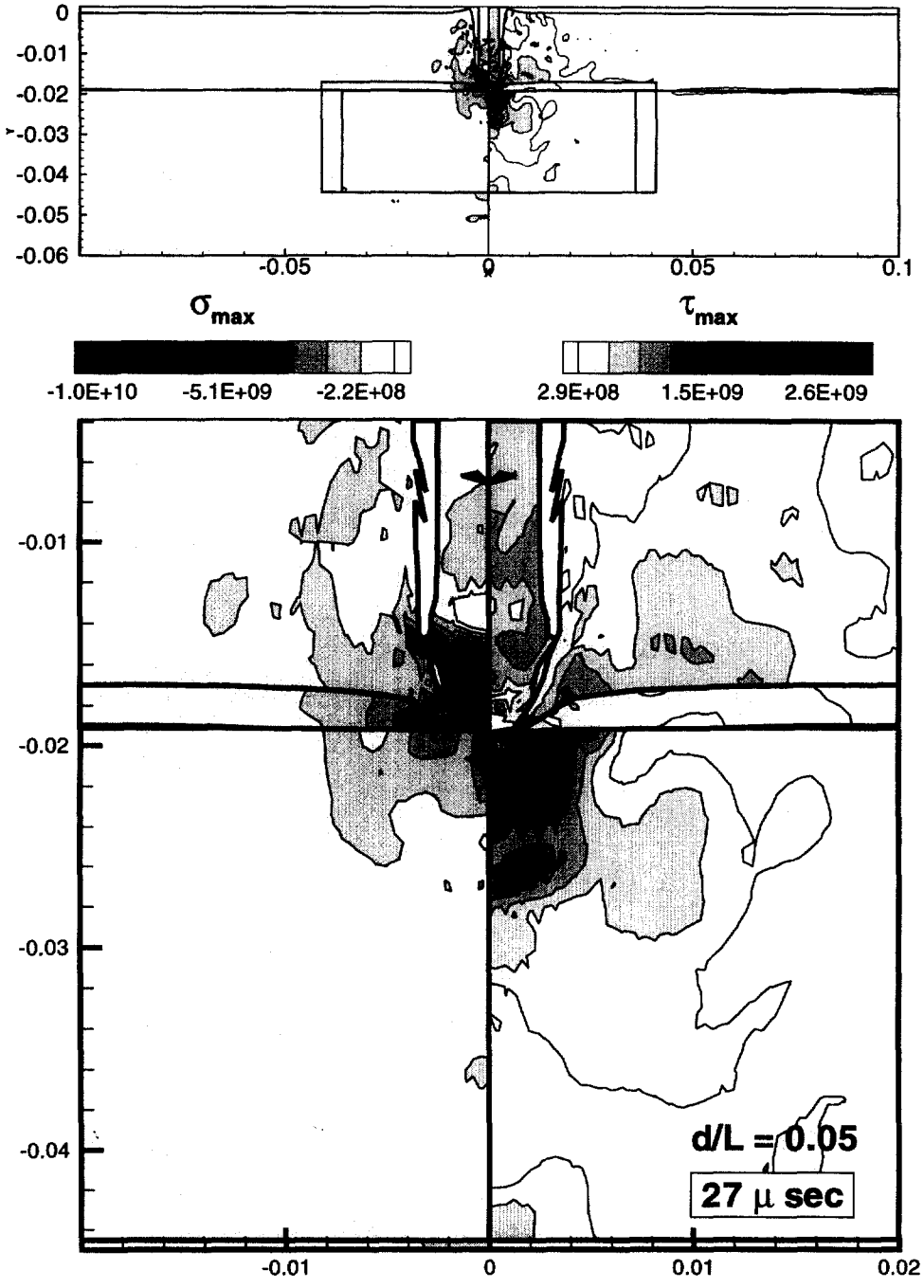

Fig. 13. Contours of maximum principal stress and maximum shear stress for the ID configuration with $d/L = 0.05$ and erosion = 1.5.

4. CONCLUSIONS

Numerical simulations of ballistic impact have been performed with a continuum damage model based on a multiple-plane microcracking model capable of capturing damage induced anisotropy and rate effects. Our effort has been focused on establishing a correlation between target material/structure systems and field variables that can be measured in penetration experiments. In the process, limitations of existing codes and challenges in material modeling, contact/interface modeling, and the need for new numerical algorithms have been identified.

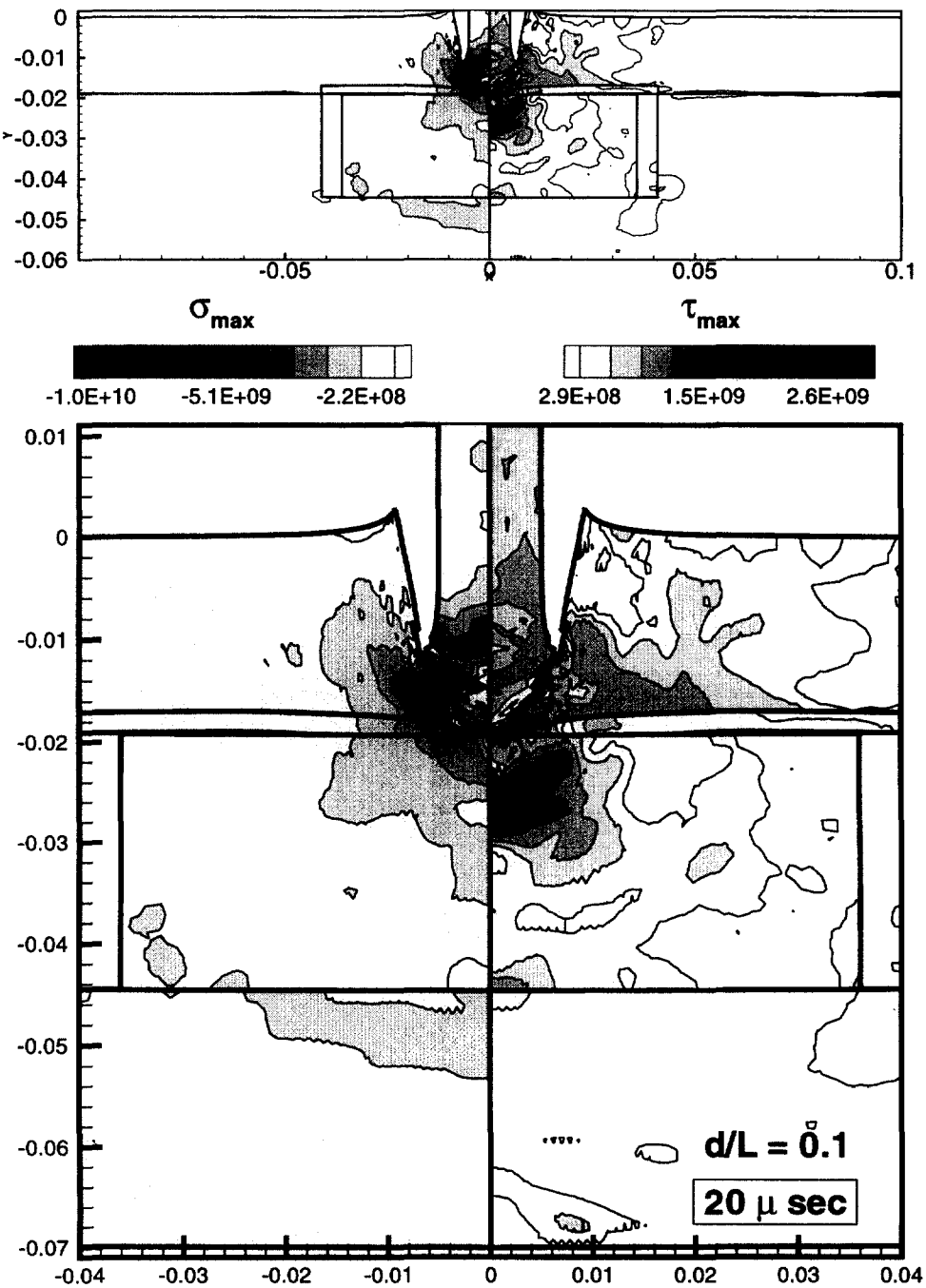

Fig. 14. Contours of maximum principal stress and maximum shear stress for the ID configuration with $d/L = 0.1$ and erosion = 1.5.

Our simulations show that the response of multi-layered ceramic targets is relatively independent of the ceramic material for the two types of ceramics considered, i.e., alumina and silicon carbide. It is shown that the development of a densely cracked zone in the ceramic ahead of the penetrator is a prerequisite for penetration. Therefore, variations in the initiation, growth, and coalescence of microcracks are expected to have an effect on the penetration process. Nonetheless, since the fragmented material must be moved out of the path of the advancing penetrator, for penetration to occur, the confinement effect provided by the steel encase appears equally important and somewhat independent of the ceramic

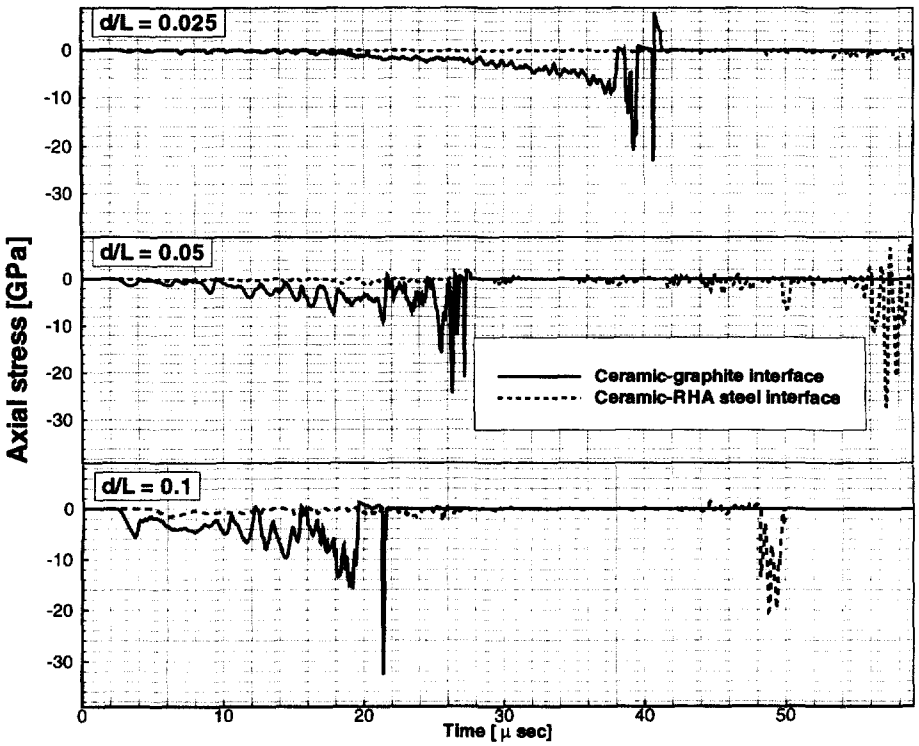

Fig. 15. Axial stress histories at ceramic–graphite and ceramic–RHA steel interfaces for ID configuration with confined alumina and different d/L ratios (erosion = 1.5).

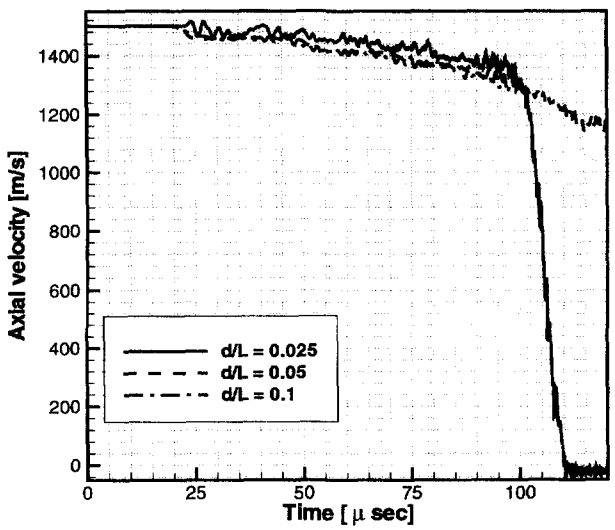

Fig. 16. Penetrator tail velocity for ID configurations with confined alumina and different d/L ratios (erosion = 1.5).

properties. We have observed experimentally, that either Al_2O_3 or TiB_2 can produce partial interface defeat of the penetrator, Brar *et al.* (1997). For these reasons, the interface defeat (ID) configuration proposed by Hauver has distinct advantages over the depth of penetration (DOP) configuration. Ceramic damage is less pronounced in the case of ID and its resistance to penetration dramatically improved by the constant confinement provided by the cover plate.

As shown by our results, the penetration process depends on the diameter to length (d/L) ratio of the penetrator for the same impact velocity. The rate of penetration increases

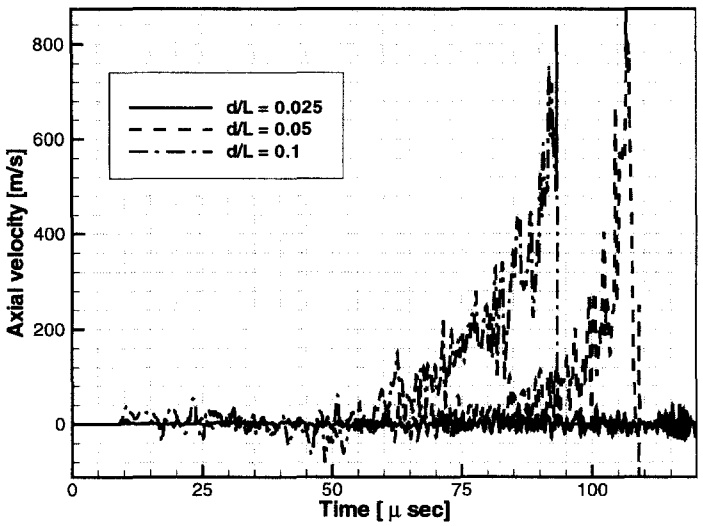

Fig. 17. Axial velocity histories at the target back surface for ID configuration with confined alumina and different d/L ratios (erosion = 1.5).

with the increase in d/L ratio. The damage zone in the ceramic plate initiates near the ceramic–graphite interface, as observed by Hauver, but the shape of the comminuted material is dependent on the d/L ratio. However, the residual velocity of the penetrator, after perforation of the ID targets, is found to be independent of the d/L ratio. This implies more ceramic damage results into more absorption of the penetrator kinetic energy. However, the peak stress is more critical for smaller values of the d/L ratio. This feature has important implications on experimental measurements and scaling issues.

Our calculations clearly show that the value of the erosion parameter is an important input for the simulation. The penetrator nose deforms and gains a conical shape as the value of the parameters is increased. This facilitates penetration and the rate of penetration increases. But, the presence of hardened material, ahead of the penetrator, reduces the velocity of the penetrator and the peak stress more efficiently. Additionally, the peak stress reverses from compressive to tensile for high erosion values. It can be concluded that the selection of an erosion parameter needs detailed experimental measurements of in-material stresses, free surface velocities and recovered penetrator shapes. All these parameters appear quite different for the range of erosion parameters investigated.

The resistance to penetration of the ID configuration appears to increase with the addition of a shock attenuator. The rate of penetration, residual velocity as well as target peak stress are reduced. This is believed to be due to the deformation and rounding of the penetrator nose while passing through the attenuator. From a design viewpoint, these observations indicate that shock stress and penetrator nose can be adjusted by tailoring the cover plates laid on top of the ceramic plate.

Several limitations have been encountered in the present analyses. We have used the same inelastic properties for both, Al_2O_3 and SiC ceramics, due to unavailability of model parameters, such as crack densities, and the critical effective cracking strain for material erosion. In addition, severe limitations have been encountered in the use of EPIC95. Only one erosion parameter can be selected for the penetrator and various target plates. Interfaces need to be modeled as perfect or frictional interfaces without the possibility of modeling progressive decohesion. Mesh adaptivity is not available to avoid excessive mesh distortion and extremely small time steps. Several contributions have been made in these areas. Ballistic penetration calculations with mesh adaptivity were performed by Camacho and Ortiz (1997). Impact simulations with adaptive meshing, using a different mesh transfer operator, were performed by Espinosa *et al.* (1996b, 1997b). These simulations show that mass conservation and mesh-size independent results can be obtained with a dynamic Lagrangian finite element code. Concerning the issue of fragmentation in brittle materials,

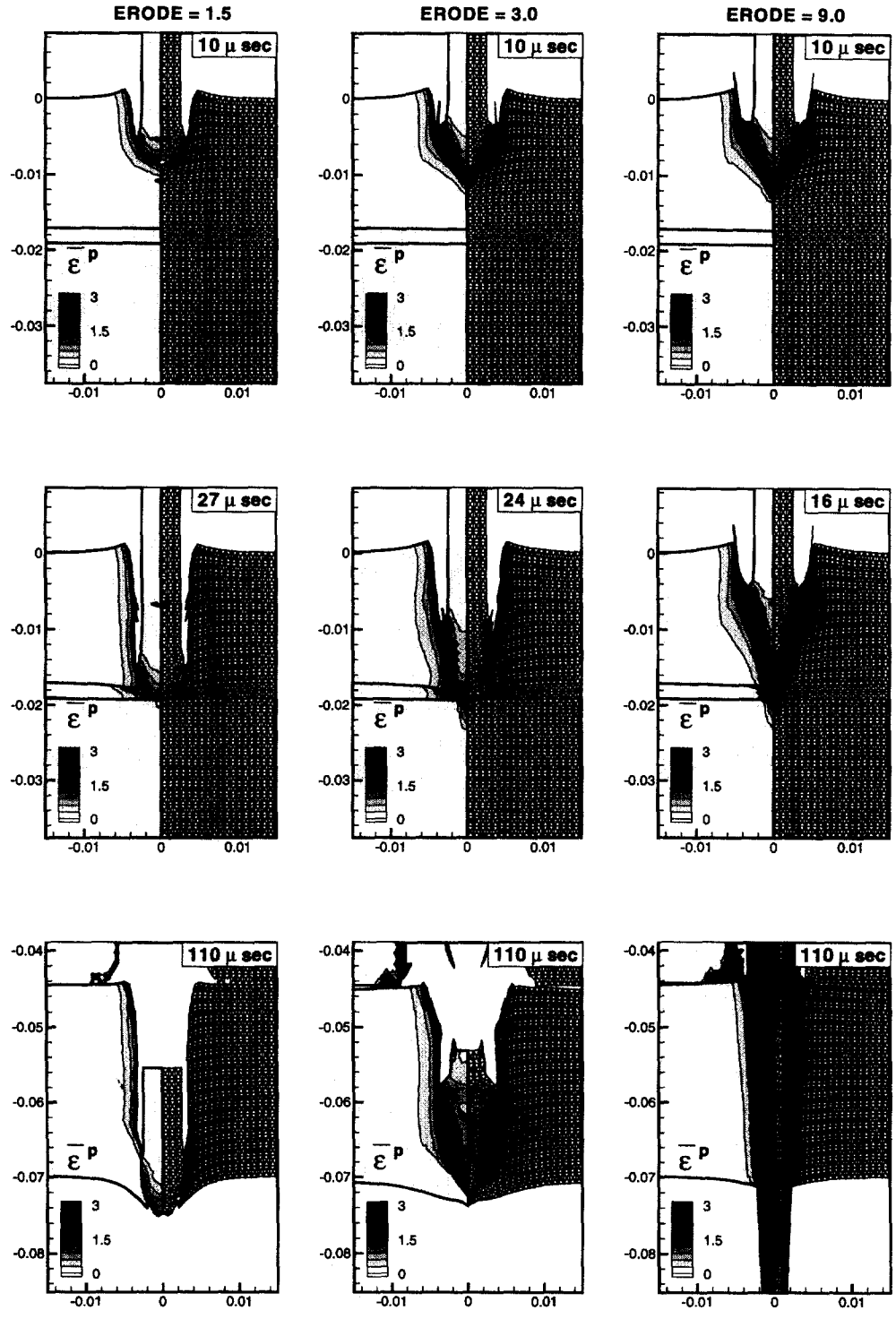

Fig. 18. Penetration and effective plastic/cracking strain for 1D configuration with confined alumina and different values of the erosion parameter ($d/L = 0.05$).

an algorithm for discrete fragmentation was derived by Camacho and Ortiz (1996). A different contact/interface formulation for fragmentation was introduced by Espinosa *et al.* (1996b, 1997b). An extension of this approach including continuum damage within fragments, which renders the calculation mesh-size independent, was derived and validated by Espinosa *et al.* (1997b). Software capable of simulating interface defeat, without ceramic

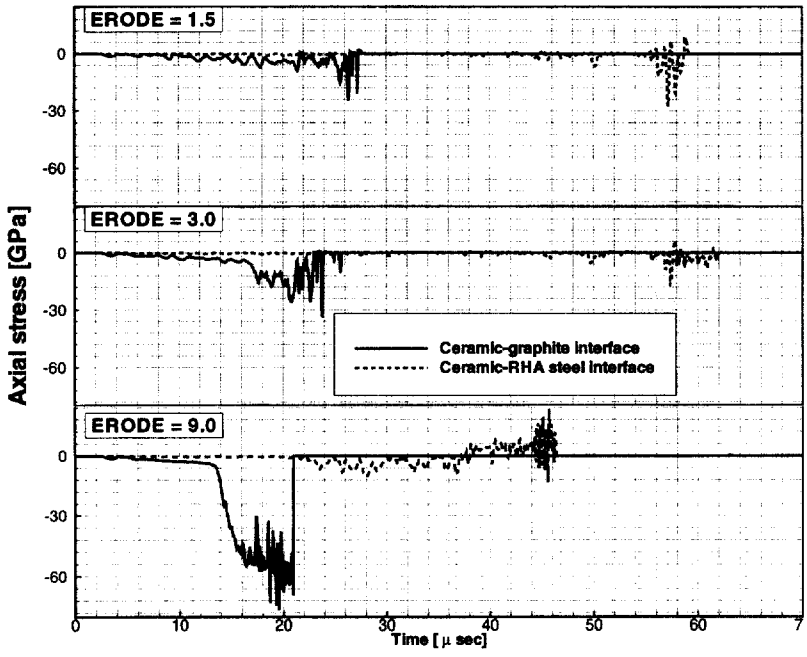

Fig. 19. Axial stress histories at ceramic–graphite and ceramic–RHA steel interfaces for ID configuration with confined alumina and different values of the erosion parameter ($d/L = 0.05$).

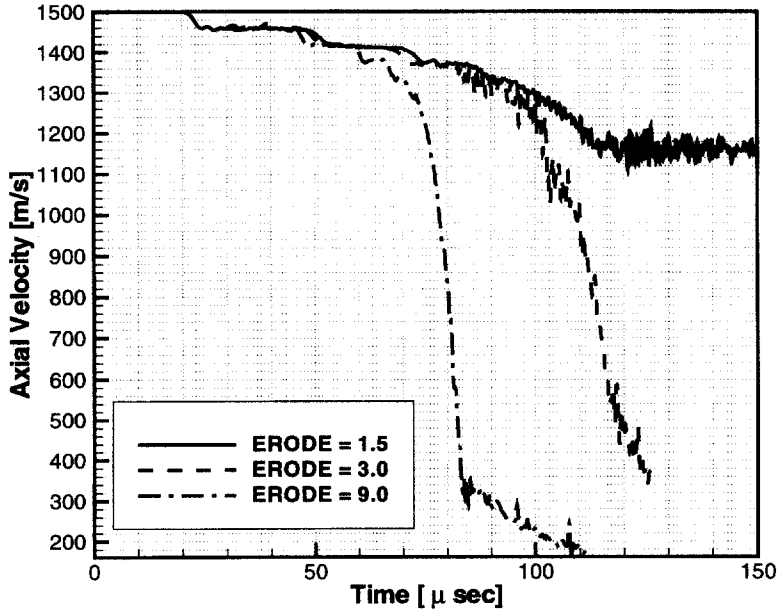

Fig. 20. Penetrator tail velocity for ID configurations with confined alumina and different values of the erosion parameter ($d/L = 0.05$).

erosion, is currently under development by Espinosa and co-workers. A combined numerical and experimental study is planned as next step to confirm the findings of this study and overcome the numerical limitations encountered in EPIC. This will help not only in establishing the various model parameters, but also aid the experimental activity being planned.

In summary, the integration of a multiple-plane microcracking model into the finite element code EPIC95 has been accomplished. The code is able to predict the response of different types of multilayered ceramic targets in confirmation with experimental evidence.

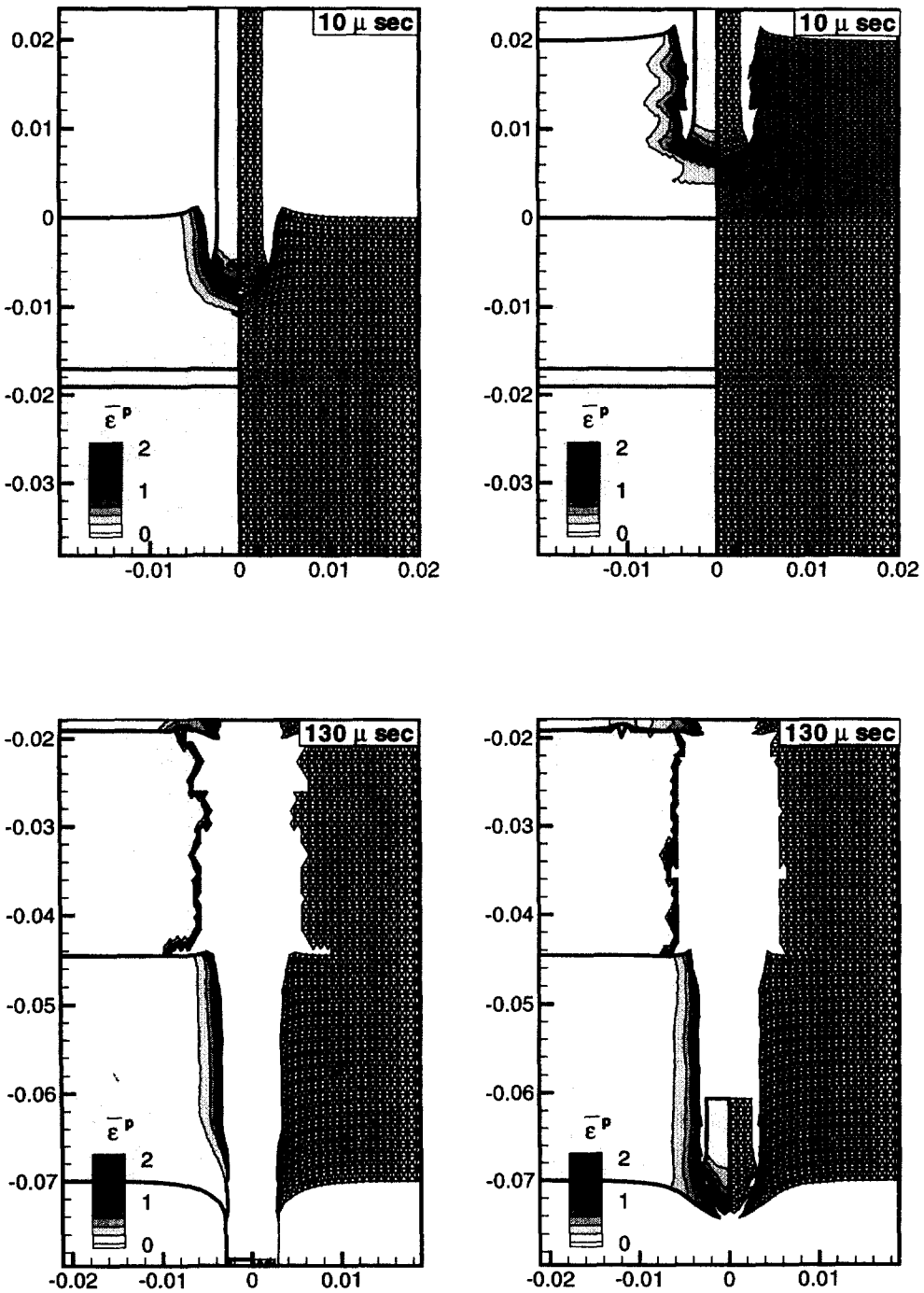

Fig. 21. Penetration and effective plastic/cracking strain with and without shock attenuator for ID configuration with confined alumina ($d/L = 0.05$, erosion = 1.5).

Although the results have been presented and compared at discrete time, the overall temporal and spatial response of the ceramic plates during penetration, has been recorded. Movies showing the formation of pressure and shear waves and their propagation, material erosion, and inertia effects resulting in an increase in crater size, even after the driving forces have ceased, have been made with the software TECPLOT. The whole process can be visualized and the numerical value of field variables retrieved, at any location and at any time, to facilitate the understanding of the penetration phenomenon and to aid in the design of lightweight armor systems.

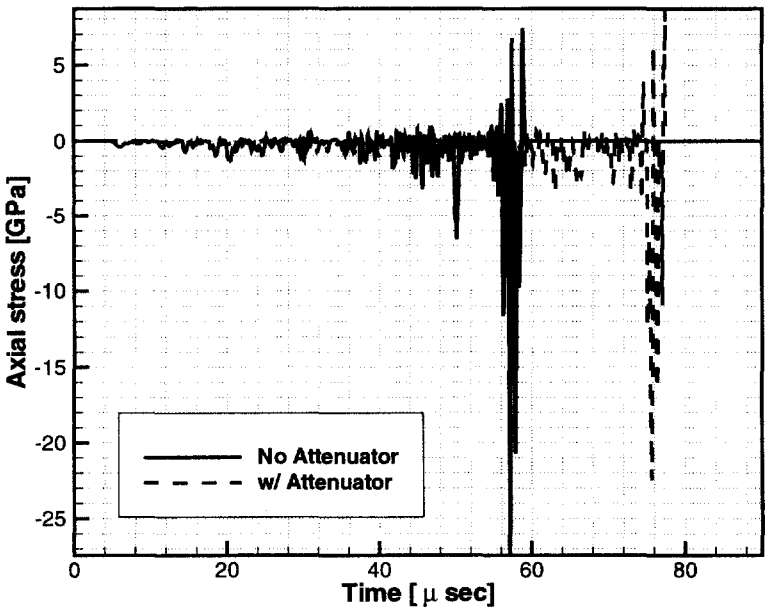

Fig. 22. Axial stress histories at ceramic–RHA steel interface without shock attenuator for ID configuration with confined alumina ($d/L = 0.05$, erosion = 1.5).

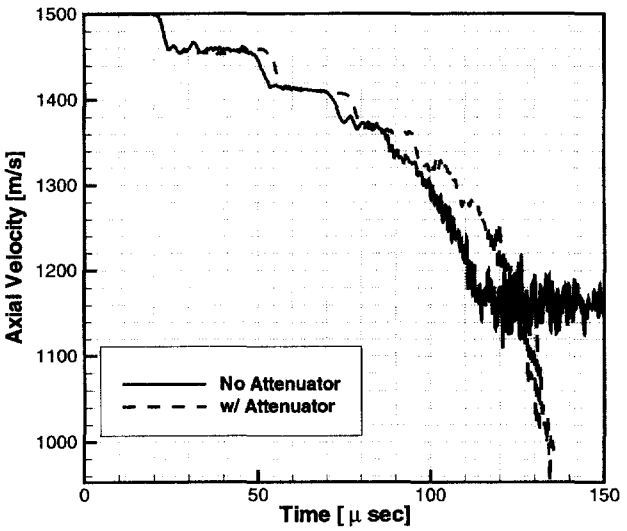

Fig. 23. Penetrator tail velocity with and without shock attenuator for ID configurations with confined alumina ($d/L = 0.05$, erosion = 1.5).

Acknowledgements—The authors are thankful to Drs Rajendran and Grove (Army Research Laboratory) for helping with the implementation of the multiple-plane microcracking model in EPIC. Many fruitful discussions were also maintained during the analyses discussed in the manuscript. This research was supported by the National Science Foundation through Grants Nos MSS-9309006, MSS 9311289, CSM-9523113, and by the Army Office of Scientific Research through award Nos DAAH04-96-1-0142 and DAAH04-96-1-0331.

REFERENCES

Addessio, F. L. and Johnson, J. N. (1989) A constitutive model for the dynamic response of brittle materials. LA-UR-89-2651, Los Alamos National Laboratory, Los Alamos, NM, U.S.A.

Brar, N. S., Espinosa, H. D., Yuan, G. and Zavattieri, P. D. (1997) Experimental study of interface defeat in confined ceramic targets. Proc. of 97 APS Topic Conf. of Shock Compression of Condensed Matter, 27 July–1 August, Amherst, MA.

Camacho, G. T. and Ortiz, M. (1996) Computational modeling of impact damage in brittle materials. *International Journal of Solids and Structures* **33**(20–22), 2899–2938.
Camacho, G. T. and Ortiz, M. (1997) Adaptive Lagrangian modeling of ballistic penetration of metallic targets. *Computer Meth. in Appl. Mech. and Engm.* **142,** 269–301.
Curran, D., Seaman, L., Cooper, T. and Shockey, D. (1990) Micromechanical model for comminution and granular flow of brittle material under high strain rate application to penetration of ceramic targets. *International Journal of Impact Engineering* **13,** 53–83.
Espinosa, H. D. (1989) Finite element analysis of stress induced damage in ceramics. M.Sc. thesis, Brown University, Providence, RI.
Espinosa, H. D. (1992) Micromechanics of the dynamic response of ceramics and ceramic composites. Ph.D. thesis, Brown University, Providence, RI.
Espinosa, H. D. and Clifton, R. J. (1991) Plate impact experiments for investigating inelastic deformation and damage of advanced materials. *Symposium on Experiments in Micromechanics of Fracture-Resistance Materials*, ed. K. S. Kim. ASME Winter Annual Meeting, pp. 37–56, Atlanta, GA.
Espinosa, H. D., Raiser, G., Clifton, R. J. and Ortiz, M. (1992) Experimental observations and numerical modeling of inelasticity in dynamically loaded ceramics. *Journal of Hard Materials* **3**(3-4), 285–313.
Espinosa, H. D. (1995) On the dynamic shear resistance of ceramic composites and its dependence on applied multiaxial deformation. *International Journal of Solids and Structures* **32,** 3105.
Espinosa, H. D., Emore, G. and Xu, Y. (1995) High strain rate behavior of composites with continuous fibers. *High Strain Rate Effects on Polymer, Metal and Ceramic Matrix Composites and Other Advanced Materials*, ed. D. S. Rajapakse and J. R. Vinson. AD-Vol. 48, ASME, San Francisco, CA, U.S.A.
Espinosa, H. D., Lu, H.-C. and Xu, Y. (1996a) A novel technique for penetrator velocity measurement in ballistic penetration studies. In *Advances in Failure Mechanisms in Brittle Materials*, ed. R. J. Clifton and H. D. Espinosa. MD-Vol. 75, AMD-Vol. 219, ASME Winter Annual Meeting, pp. 23–48, Atlanta, GA.
Espinosa, H. D., Zavattieri, P. D. and Emore, G. L. (1996b) Computational modeling of geometric and material nonlinearities with application to impact damage in brittle failure. In *Advances in Failure Mechanisms in Brittle Materials*, ed. R. J. Clifton and H. D. Espinosa MD-Vol. 75, AMD-Vol. 219, ASME Winter Annual Meeting, pp. 119–162, Atlanta, GA.
Espinosa, H. D., Lu, H.-C. and Xu, Y. (1997a) A novel technique for penetrator velocity measurement in ballistic penetration studies. To appear in *Journal of Composite Materials*.
Espinosa, H. D., Zavattieri, P. D. and Emore, D. (1997b) Adaptive FEM computation of geometric and material nonlinearities with application to brittle failure. To appear in *Mechanics of Materials*.
Freund, L. B. (1990) *Dynamic Fracture Mechanics*. Cambridge University Press.
Gurson, A. L. (1977) Porous rigid-plastic materials containing rigid inclusions—yield function, plastic potential and void nucleation. In *Adv. Res. Strength Fract. Matls.* 2*a*, ed. D. M. R. Tablin. Pergamon Press, NY, U.S.A.
Hauver, G., Netherwood, P., Benck, R. and Kecskes, L. (1993) Ballistic performance of ceramic targets. *Proceedings of Army Symposium on Solid Mechanics*, 17–19 August, Plymouth, MA, U.S.A.
Hauver, G., Netherwood, P., Benck, R. and Kecskes, L. (1994) Enhanced ballistic performance of ceramics. *19th Army Science Conference*, 20–24 June, Orlando, FL, U.S.A.
Johnson, G. R. (1976) Analysis of elastic–plastic impact involving severe distortions. *Trans. A.S.M.E., J. Appl. Mech.* **98,** 439–444.
Johnson, G. R. and Cook, W. H. (1985) Fracture characteristics of three metals subjected to various strains, strain rates, temperature and pressure. *Eng. Frac. Mech.* **21,** 31–48.
Johnson, G. R. and Stryk, R. A. (1986) *User Instruction for the EPIC-2 Code*, AFATL-TR-86-51.
Johnson, G. R. and Stryk, R. A. (1987) Enroding interface and improved tetrahedral element algorithms for high velocity impact computation in three dimensions. *International Journal of Impact Engineering* **5,** 411–421.
Johnson, G. R., Stryk, R. A. *et al.* (1994) *User Instructions for the* 1995 *Version of the EPIC Research Code.* November 1994, Alliant Techsystems Inc., 600 Second Street N.E., Hopkins, MN 55343.
Klopp, R. W. and Shockey, D. A. (1991) The strength behavior of granulated silicon carbide at high strain rates and confining pressure. *Journal of Applied Physics* **70**(12), 7318–7326.
Needleman, A. (1988) Material rate dependence and mesh sensitivity in localization problems. *Comput. Meth. App. Mech. Engng* **67,** 69–85.
Orphal, D. L. and Franzen, R. R. (1996) Penetration of confined aluminum nitride targets by tungsten long rod at 1.5–4.5 km/s. *International Journal of Impact Engineering* **18,** 355–368.
Orphal, D. L. and Franzen, R. R. (1997a) Penetration of confined silicon carbide targets by tungsten long rod at impact velocities from 1.5–4.6 km/s. *International Journal of Impact Engineering* **19,** 1–13.
Orphal, D. L., Franzen, R. R. and Charters, A. C. (1997b) Penetration of confined boron carbide targets by tungsten long rods at impact velocities from 1.5–5.0 km/s. *International Journal of Impact Engineering* **19,** 15–29.
Ortiz, M. (1996) Computational micromechanics. *Computational Mechanics* **18,** 321–338.
Rajendran, A. M. and Grove, D. J. (1992) Modeling the impact behavior of AD85. Proceedings, 24th Int. SAMPE Tech. Conf., Allied-Signal Inc., Oct. 1992.
Rajendran, A. M. (1992) High strain rate behavior of metals, ceramics and concrete. Air Force Report WL-TR-92-4006. Wright-Patterson Air Force Base, OH, U.S.A.
Rapacki, E. J., Hauver, G. E., Netherwood, P. H. and Benck, R. (1996) Ceramics for armors—a material system perspective. 19th Annual TARDEC Ground Vehicle Survivability Symposium, 26–28 March, 1996, Monterey, CA, U.S.A.
Sairam, S. and Clifton, R. J. (1994) Pressure–shear impact investigation of dynamic fragmentation and flow of ceramics. ASME AMD-Vol. 197, *Mechanical Testing of Ceramics and Ceramic Composites*, ed. A. Gilat, pp. 23–40.
Sandler, I. S. and Wright, J. P. (1984) Strain-softening. *Theoretical Foundations for Large Scale Computations of Nonlinear Materials Behavior*, ed. Sia Nemat Nasser *et al.*, p. 285.
Shockey, D. A., Marchard, A. H., Skaggs, S. R. *et al.* (1990) Failure phenomenology of confined ceramic targets and impacting rods. *International Journal of Impact Engineering* **9**(3), 263–275.
Steinberg, D. (1992) in *Shock Compression of Condensed Matter*—1992, pp. 447–450. Elsevier Science Pub., B.V.
TECPLOT, *Version* 6 *User's Manual.* Amtec Engineering Inc., P.O. Box 3633, Bellevue, WA 98009-3633.